# UoA Undergraduate Mechatronics Research Journal

Volume 6 • December 2013

A Publication of Mechatronics Engineering Group,
Department of Mechanical Engineering,
The University of Auckland, New Zealand

ISSN 1171-9494

# UoA Undergraduate Mechatronics Research Journal



*UoA Undergraduate Mechatronics Research Journal* is published annually by the Mechatronics Engineering Group of the Mechanical Engineering Department, The University of Auckland, 20, Symonds Street, Auckland, New Zealand.

# Preface

Mechatronics research basically integrates on mechanical, computer and electrical engineering for innovation of smart devices, machines, systems and production processes. At the University of Auckland, we focus on the systems design and integration using mechanisms, sensors, actuators, controls, computers and real-time software, with primary applications into healthcare, medicine, sports, manufacturing and agricultures.

The Bachelor of Engineering (Hons) in Mechatronic Engineering was launched in 2002. As part of the degree requirements, the fourth year students, in a pair, need to complete a research project, or Final Year Research Project (FYRP).

FYRPs represent also our academic staff members' research activities. This journal is an avenue for students to publish their FYRPs. Since the contribution to the journal is voluntary, this issue of nine papers only showcases our student research programme.

Wish all of you enjoy reading this issue.

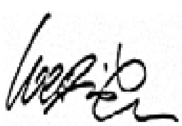

Peter Xu
*Professor & Chair of Mechatronics Engineering*

# Table of Contents

# Investigation into Fibre Optic Technology for Tactile Sensing in Minimally Invasive Surgery

Harriet Peel, Suzanne Bell
The University of Auckland,
Department of Mechanical Engineering,
Mechatronics Engineering,
New Zealand

## Abstract:

Surgical intervention, often including the insertion of pedicle screws into the vertebrae, remains a common treatment for a number of orthopaedic conditions, including scoliosis and external trauma to the spine. Minimally invasive surgery uses small incisions to access the surgical site, to minimize soft tissue trauma to the patient. The insertion of hardware into the spine during surgery is made increasingly perilous with the advent of these minimally invasive techniques. This study investigates the viability of a hand held tool with a Fabry Perot Interferometry based sensor embedded to provide feedback to the surgeon of the tool's location within the vertebrae. Three tool designs were constructed and tested. The optimal design was capable of bearing the forces reasonably expected in surgery, and reported a positive linear relationship between applied force and voltage increases, across a 4N force range.

**Keywords:** Fabry-Perot, Orthopaedic Surgery, Fibre-optics, force sensing,

## 1. Introduction

The aim was to develop a working prototype surgical tool with remote tip tactile sensing for Minimally Invasive Spinal Surgery, specifically pedicle screw implantation.

Pedicle screw implantation is the surgical procedure where screws are inserted into the pedicles of the vertebrae,, in order to create a stabilising structure across vertebrae. This allows a number of spinal conditions, such as fractures, to be treated [1]. Traditionally, this surgical procedure is performed as an "open" procedure; one long entry incision is made in order to access the spine, while avoiding the nearby nervous system. However, these methods are physiologically taxing to the patient, with significant blood loss and tissue damage ensuing. This also leads to significant post-operative care requirements [2].

Minimally Invasive Spine Surgery (MISS), is the spinal procedure where the operation site is accessed via small incisions, thus reducing tissue damage and blood loss. While successful MISS does improve patient outcomes, the surgery is challenging for the surgeon; the small incisions reduce the opportunity for visual feedback and the smaller tools and relatively larger tissue forces reduce haptic information to the surgeon. This information is crucial to aid the surgeon in providing a safe and accurate screw positioning [3] .

Fabry Perot Interferometry (FPI) is a Magnetic Resonance Imaging (MRI), heat and chemical resistant sensing system which holds promise as part of a surgical tool which can penetrate the bony tissue of the spine and respond to contrast in tissue variations [4]. A response to tissue variations can be interpreted to identify the harder outer bone, which lies close to the fragile nerves and spinal cord. In a 2012 study a single test of an FPI sensor was embedded in a pedicle probe, showed detection of force variation provided by between 0 and 150g of mass. However, the expected loading undergone in orthopaedic surgery could not be withstood by this design. . The objective of this study was therefore to advance the initial 2012 design to a working prototype that can withstand and quantitatively identify the variation in the 2-20N forces expected during spinal surgery [5].

## 2. Working Principle

The FPI optical sensor consists of two fibre optics, an incidence fibre, and a secondary fibre (Figure 1). The two fibres are fixed inside a glass capillary using glue or a hot splice, with a gap between the right angled cleaved fibre ends, which act as translucent mirrors. Some of the light from the incident fibre reflects off the cleave (R1) and some transmits through the end of the incident fibre and is reflected back into the incident fibre by the secondary fibre (R2). A portion of light is transmitted through the cleaved end of the secondary fibre and is dissipated. There is a fractional time delay between the reflection of light from the cleave of the incident fibre, and the reflection of light from the second fibre and therefore there exists a phase difference between the two light beams. This combines once the light is returned to the incident fibre and dictates the intensity of the returning light beam. Once load is applied to the secondary fibre, the gap between fibres changes, changing the phase difference and the intensity of the returning light. Equation 1 was used to convert the air cavity into a phase change:

$$\Delta\emptyset = \frac{2\pi \vartriangle d}{\lambda} \qquad (1)$$

where δ is the change in cavity size in meters, and the $\lambda$ is the wavelength (1550nm in this study to minimise light attenuation). This can then be converted into a light intensity.
Equation 2 models the intensity of this combined light:

$$I = I_1 + I_2 + 2\sqrt{I_1 I_2}\cos(\Delta\emptyset) \qquad (2)$$

Where $I_1$ and $I_2$ are the intensities of the reflected beams at R1 and R2. The light intensity relative to force follows a sinusoidal curve.

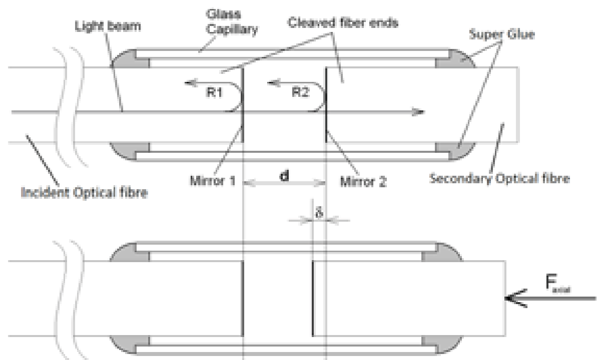


Figure 1. Fabry Perot Interferometry Sensor

## 3. Sensor Development and Testing

The pedicle probe with embedded FPI sensor in the previous study was not capable of withstanding loads greater than 1.5 N. Therefore, three different probe designs were developed, in order to maximise the strength of the probe, and retain maximum sensitivity. Probe A made from medical grade stainless steel was consistent with the previous design; a 70mm long rod of 4mm diameter has a groove 1 mm (W) x 2.4 mm (D) along its length. The sensor and fibre are embedded in the groove using epoxy resin, with the sensor tip protruding at the probing end. Probe B was a similar probe; however the sensor was embedded using soft caulk silicon filler (shown black in Figure 7) while the fibre was held in place using the epoxy resin. The final Probe C, to protect the glass end of the sensor, has a 0.5 mm thick steel cap at the embedded sensor's tip.' The sensors were built using 125 µm fibres glued into a glass capillary as described previously.

## 4. Sensor Testing

The test rig includes a sliding platform, which sits on top of the sensor tip and is weighted to imitate the loads in surgery. The bare sensor is held in place below the platform by a collet, while the newly developed probes, too large for this design, were held in this location using a ring vice, constructed from nylon and a grub screw. Three tests were carried out.

Test 1: Cumulative Loading of the Sensor

The aim of this test was to measure the change in output voltage when the sensor is loaded. Both the bare sensor and the sensor in two probe designs were tested by progressively adding 50g weights to the sensor at one minute intervals. This was to observe the response of the sensor to force, as well as to observe the response lag of the set up. During this test, the sensor which is protected by the steel and epoxy probe could endure higher loads without the concern that the glass capillary would shatter as more weight was required to deform the capillary. The maximum weight applied to the bare sensor was 150g (1.47N), whereas the maximum load applied to the steel encased sensors was 2.3kg (22.6N). The loading of the steel probes above 1.47N was undertaken as a separate, final test after the following tests were undertaken, in order to reduce the chance of probe failure before this study was completed.

Test 2: Dynamic Testing; power measurement.

The aim of this test was to establish the effect of constantly changing load (immitating what the tool would undergo in surgery), as well as the sensor's recovery, by steadily increasing the load on Probe A from 0 to 600g over a period of five minutes, and then steadily reducing the load over five minutes. Initial tests showed that the effects of circuit noise was exacerbated by the constantly changing load, therefore a power meter was used, to measure the light intensity at the sensor instead of through the LabView programme.

Test 3: Temperature Test

Although the literature reported that the sensor itself was thermally resistant, and the borosilicate glass has a very low coefficient of thermal expansion ($\sim 3 \times 10{-}6$ /°C at 20°C) it was observed that if the sensor probe was in contact with a warmer object for a long period, the voltage would slowly climb. In response to this observation, a test was conducted where the probe was heated for a period of one minute and then immediately cooled (to maximise temperature gradient) over the same time interval, and the voltage reading at each minute was recorded.

## 5. Results and Discussion

### Test 1: Bare Sensor

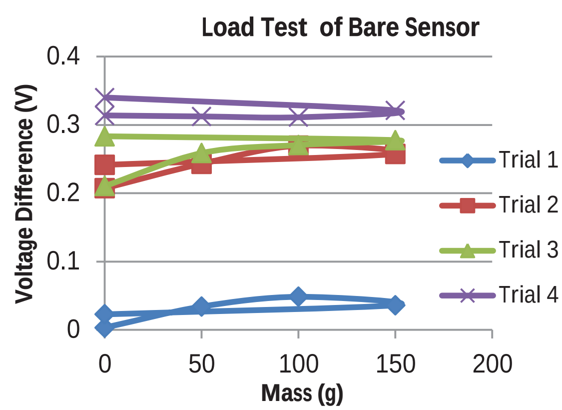


Figure 2. Voltage Response of Bare Sensor as load is increased from 0g to 150g

In trials 1-3, as weights are applied from 50 to 100g, the voltage increases until 150g is added, then the voltage reading drops (Figure 2). In trial 4, the sensor response is almost linear.

This indicates that the air cavity between the two mirrors in the sensor is such that the light reflected from mirror 2 is already out of phase with light from mirror 1, as weight is added the light waves interfere constructively and then destructively, or the sensor is operating in green area indicated in Figure 4.

During the first three trials, once the weight is removed, the final voltage is higher than at the commencement of the test. The increase in voltage difference at zero loads between the start and end of the test can be attributed to creep of the sensor, where the adhesive does not recover entirely from each loading sequence, thus the air cavity does not return to its original size. This is further confirmed by Trials 3 and 4, where the increase in voltage difference per unit load is reduced, compared with earlier tests. It is believed that this is caused by compression of the glue bond, which was reducing the ability of the air gap to deform. As trials were repeated, in this test, the load was not increased beyond 150g, to avoid shattering the capillary or shearing the glue in its unprotected state, as after this point, some permanent shifting of the fibre within the capillary was observed. This permanent deformation also provides some explanation to degradation of the relationship between force and voltage in later trials, as the probe's ability to deform further was reduced. Due to the time consuming nature of rebuilding the sensors, deliberate testing to failure was avoided within this study.

Test 1: Open Probes

For the open probe A, there is approximately linear voltage response to the steadily increasing load, with some disturbance at 300g (Figure 3). Furthermore, over each range of 150g, there is a voltage increase of circa 0.0325 volts. This is half of the voltage response of the bare sensor over a similar range, and thus shows that steel probe structure absorbs some force, and reduces the deformation of the sensor.

However, probe B and C both record no variation over this test. For Probe C this can be attributed to high which prevents the capillary from deforming sufficiently and therefore no voltage response is recorded. Conversely, the very soft silicon filler used to protect the sensor in Probe B appears to absorb the applied load to the point where the capillary does not deflect and register a reading. Further testing of Probes B and C was not carried out, as neither probe showed significant response to load.

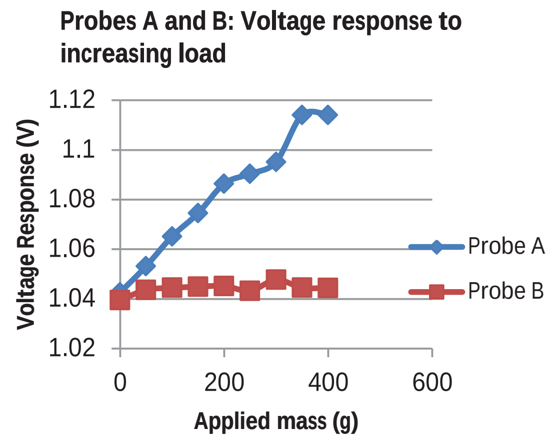


Figure 3. Voltage response of Probes A and B to steadily increasing load (Test 1).

In subsequent tests of Probe A, the linear response to increasing load was repeated (Figure 4). However, the incremental change is significantly less than in the initial tests (a voltage increase of 0.01 V per 4N increase) is significantly less than in the initial test a voltage increase of 0.08 V per 4N increase), and the curve only increases significantly with every second weight addition – a total mass increase between voltage response of 100 g. This was indicative of permanent probe damage, and would imply that the probe had been deformed in the initial test, and potentially not recovered this deformation. Therefore, the range of deformation for subsequent tests was reduced.

In the final test conducted on probe A, using higher loads (up to 2.3kg or 22.6 N), the probe continues to record an increasing voltage response with increased load (Figure 5). However, this test was the last test conducted and as with the previous trials the overall voltage response is significantly reduced (even with the additional load). This indicates that the top of the typical sinusoidal force curve is being approached as load increases and thus reducing the incremental voltage response or the probe has undergone damage during testing.

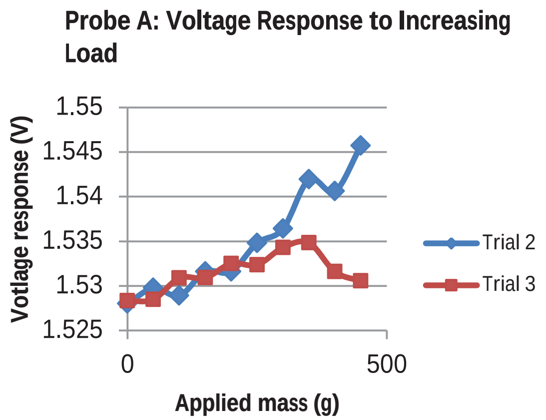


Figure 4: Subsequent load testing of Probe A (Test 1).

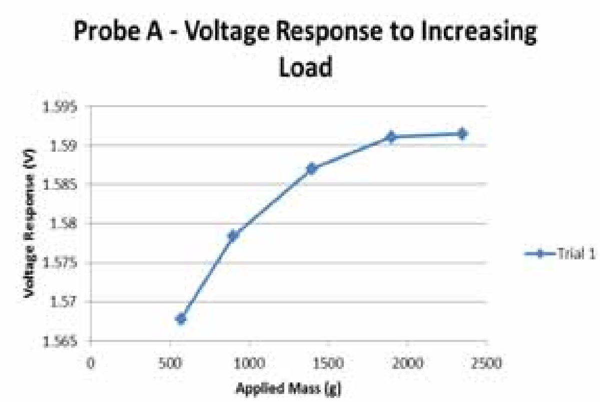


Figure 5: Probe A Response to Increasing Load at increased load range.

Test 2: Dynamic Test

The dynamic test shows that as the load on the open probe sensor is steadily increased from 25g to 500g, the light intensity as measured by the power meter records a drop from 8.44 to 7.86 microwatts. Conversely, as load is removed, the power meter records an increase in light intensity from 7.83 to 8.37 microwatts (Figure 6). This is a change in curve direction from that observed in the preceding tests, indicating that the probe had undergone some permanent deflection,

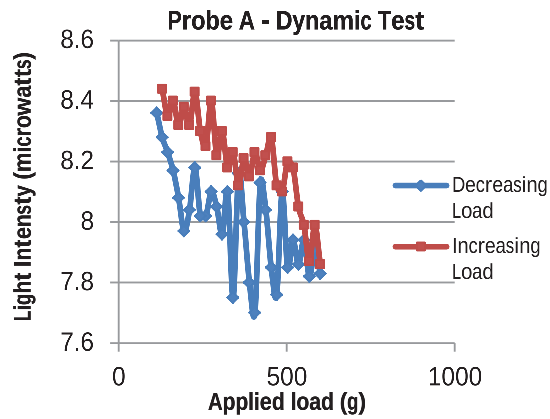


Figure 6. Intensity response to constantly changing load

during the testing process, and therefore operated in a different (now down ward sloping) area of the curve, compared to earlier trials.

The jagged variation in readings observable over the course of this test is caused by several factors, including the effect of ambient light entering the fibre. The variation also shows the influence of vibrations as the weights are added and removed. During the test, loads were added and removed manually, and the rig was disturbed more in the collection of the weights than during their deposition.

As observed in the bare sensor test, the light intensity returned from Probe A does not return to its original level after initial loading, thus, voltage response during the decreasing load testis consistently higher than the first test. It also illustrates that the sensor is not recovering its gap entirely.

Another explanation for the overall voltage increase is increased resistance in the amplification circuit as the components heat up over time, a large amplification has been used making it more susceptible to increased resistance as the circuit warms.

Test 3: Temperature Test

As the temperature of Probe A is increased and decreased, there is a periodic response to (A control graph, without deliberate temperature changes shows that this is not the result of other variation) (Figure 7). As the probe is heated (shown as the pink zone in Figure 7), a slight climb in voltage, or reduced drop in voltage is observed, and when cooled (the green zone), a significant drop in voltage is repeatedly observed. From this it has been inferred that as the steel probe is heated and cooled the steel is expands and contracts, and thereby deforms the sensor. It is also interesting to note that the sensor responded less to expansion due heat than contraction. This may be attributable to the fact that the temperature gradient from the heated sensor to the cooled sensor is larger than that which occurs as the sensor is raised from room temperature. In terms of the surgical application of the tool, the temperatures reached by the probe (>60ºC during heating, < 7 ºC during cooling) far exceeded those reasonably expected in a surgical environment. However, this does prove that as the sensitivity of the sensor is increased and calibrated, the effect of body temperature versus air temperature requires consideration. Consideration may also be needed to the effect of high-temperature tool sterilisation.

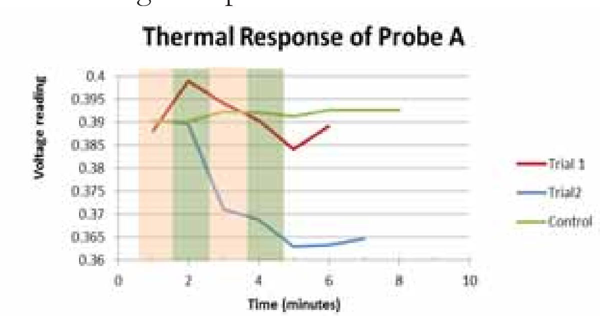


Figure 7. Voltage response of Probe A to variations in temperature.

## 6. Conclusions

1. The sensor embedded in open steel probe enabled the sensor to function under loads up to 23 N, as per the study's objective. However repetitive tests initiated plastic deformation of the sensor, which reduced the voltage response range at higher loads.

2. Physical testing showed that the steel encased sensor could provide a semi linear (and therefore easily calibrated) response to load over a range of approximately 4N.

3. Precise calibration was not possible within the bounds of this study for three reasons:
    a. The construction method was insufficiently precise to ensure that the sensor gap provides a predictable response on the sinusoidal voltage curve.
    b. The sensors degrade over repetitive tests, making any calibration invalid after multiple tool uses.
    c. Circuit noise means real-time sensor response is yet to be achieved.

## 7. Future Work

There is much to be improved in the area of sensor construction. Splicing the fibre to the capillary would provide one means of improving sensor performance, in keeping with previously proven designs in the literature. Furthermore, since the sensor is intended to bear large compressive loads, the use of a glass capillary in the sensor is not ideal, due to its propensity to shatter. While further materials research could provide an alternative to glass capillary,

**Figure 8.** Proposed new design for sensor.

Figure 8 illustrates an alternative design to reduce loads on the glass componentry. This design proposes that the structural integrity of the probe itself is made dependent on the steel probe, by bonding the fibres and capillary to the steel individually. With this design, the change in air cavity is not dependent on the deformation of the glass capillary, rather, as the steel compresses, the fibres would slide together within the glass, with the capillary acting only to align and protect the fibre tips. It is believed that this would increase the change in air gap length per unit force, as the total strain on the steel is utilised and thereby improve the distinction of the varying forces, as well as reduce the load on the fragile capillary.

## Acknowledgements

The authors are grateful to Professor Peter Xu and Professor Neil Broderick for their expert supervision, as well as Dr. Peter Robertson of Ascot Hospital for his support of the project.

## References

[1]. Weinstein, J.N., Rydevik, B.L., and Rauschning, W. (1992). Anatomic and technical considerations of pedicle screw fixation. *Clinical Orthopaedics and related research*, *284*, 34-46.

[2]. Zeiller, S.C., Lee, J., Lim, M., and Vaccaro, A.R. (2005). Posterior thoracic segmental pedicle screw instrumentation: evolving methods of safe and effective placement. *Neurology India*, *53*(4), 458.

[3]. O'Dowd, J.K. (2007). Minimally invasive spinal surgery. *Current Orthopaedics*, *21*(6), 442-450

[4]. Singh, J., Potgieter, J., Xu, X.L. Fiber Optic Force Sensor for Flexible Bevel tip Needles in Minimally Invasive Surgeries.

[5]. Heinen, A. and Dasgupta, S. (2012). A Smart Surgical Tool for Minimally Invasive Spinal Surgery (MISS). *UoA*, 32.

# ReachHab: A bilateral upper limb rehabilitation device for stroke

Hannah Sheahan, Emily Maxwell
The University of Auckland,
Department of Mechanical Engineering,
Mechatronics Engineering,
New Zealand

## Abstract:

Recently bilateral exercises and robotics have been shown to assist upper limb motor control relearning after stroke. The purpose of this study was to design and test the potential of a new rehabilitation tool, the ReachHab, for improving bilateral upper limb reaching from a sitting position in stroke patients. Based on an identified clinical need, the three-degree of freedom system was designed for the user to move a pivoting handlebar around an angled sliding platform to imitate a task-specific reach. The applied force imbalance between arms could be monitored to quantify the degree of disparity between the paretic arm and the contralateral arm while producing this motion. This information was then relayed to an iPad system for visual monitoring. Three-dimensional joint kinematics were monitored on one healthy 65-year old participant while using the ReachHab. Anterior shoulder and elbow flexion were successfully targeted to produce a characteristic kinematic reaching action.

**Keywords:** stroke, rehabilitation, upper-limb, reach, shoulder.

## 1. Introduction

As the leading cause of long-term disability in adults, stroke remains a major global public health concern. [1-3] Humans have a remarkable ability to learn motor tasks, yet with nearly 77% of patients demonstrating symptoms, upper limb (UL) motor deficit is the most common complication following acute stroke. [4]

Anterior shoulder flexion is a basic functional requirement of the arm for producing an accurate reach-to-grasp action. The coordination of anterior shoulder and elbow flexion and extension is particularly important and causes additional difficulties in stroke rehabilitation. [4]
Despite this, continued UL impairment prevails in 50 - 95% of stroke patients treated using traditional therapies, meaning more effective therapeutic approaches should be sought. [5]

Wu et al's 2012 clinical trial found that robot-assisted bilateral arm training may be more beneficial than therapist-based rehabilitation for improving shoulder flexion after stroke, [6] while a 2007 randomised control trial by Masiero showed that patients who received UL robotic therapy in addition to conventional post-stroke therapy showed greater reductions in motor impairment and improvements in functional ability than traditional therapy alone. [7]
Robotic sensorimotor devices have been proven to improve functional motor outcomes in the elbow and shoulder, yet few devices have been made affordable or commercialised beyond the prototyping stage. [8] Finally, bilateral UL exercises have been supported through systematic reviews for offering improved functional motor gains following stroke over their over unilateral counterparts, yet few bilateral rehabilitative devices have been designed or adequately tested for functional improvements in their users. [10-12]

This report details the development and testing of a bilateral robotic rehabilitation system for improving functional UL reaching in patients following a stroke. The project was undertaken by the Department of Mechanical Engineering at the University of Auckland in conjunction with the Laura Fergusson Rehabilitation centre, to begin developing an UL system that targets appropriate physiological factors.

## User-centric Design

Industry experts in rehabilitation healthcare devices, stroke physiotherapy, and medical device manufacturing were consulted in order to construct a House of Quality assessment to prioritise these requirements. The targeted patient group was identified as those scoring at MAS level 4 or above in the Upper Arm Function and Hand Movements sections, meaning the user has the ability to hold their arm straight out in front for two seconds on their own after it has been positioned there by a physiotherapist.

A diagram of the complete system can be seen in Figure 1. The design entails a system that uses a magnetic rotary encoder to measure the z-rotation of a handlebar along an x-y slider plane, to quantify the torque imbalance from two hands pushing or pulling on the handlebar about its centre. The design is intended for use by patients pushing the handles up along an elevated planar x-y slider to their full UL range of motion, before bringing the handles back to their original position or another position on the plane. A visual monitoring system will constantly record the force imbalance between the user's arms and award game points only when the arms are outputting forces within a range of each other specified by the physiotherapist for the particular patient - to ensure the disabled arm receives the intended benefit of the exercise, and that the difficulty level is appropriate for the patient.

## Ergonomics and Anthropometry

Anthropometric estimates from Pheasant and Haslegrave for 65 -80 year old adults gave information on: UL range of motion from a sitting position; screen height and angle; range of vision; handle positions, size and angles. [13]

The 5th and 95th percentile shoulder-grip lengths and sitting shoulder heights were taken to design the device around the range of reach for healthy users. The slider reach of 373mm x 190mm shown in Figure 1 was designed around work space ergonomics such that the device requires only natural range of motion extensions used in everyday tasks.

The position and angles of handles were based off the neutral wrist position for reaching and grasping of 10-20° of ulnar deviation, 90° pronation. To accommodate the fact that upper extremity weakness affects up to 76% of stroke patients, the intensity of the exercise can be adjusted by raising or lowering the angle of inclination α, of the slider platform. [14] Raising the platform will increase the vertical travel distance of the slider when moved in the y-direction, meaning the user will be working harder against gravity and this movement will require greater strength.

Primarily, flexion and extension of the shoulder and elbow were the targeted kinematic movements for patients using the ReachHab. By moving the handlebars diagonally or in circles within the x-y plane, external and internal shoulder rotation can also be achieved. More complicated shoulder rotation movements involving adduction and abduction, as well as elbow supination and pronation can be achieved by tracing alternate paths with the handlebars.

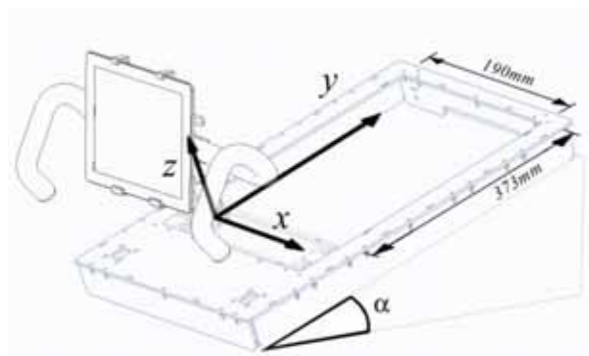


Figure 1. The ReachHab slider and rotation coordinate system

## Quantifying Upper Limb Disparity

To ensure the strong arm does not dominate physiotherapy, and to provide accurate patient improvement data to the physiotherapist, the ReachHab was designed to clearly quantify the apparent disparity in ability between the paretic arm and the capable arm.

This was achieved by allowing limited rotation around the z-axis of the handlebars. Built into the handlebar and iPad support of the ReachHab is a system comprising a silicon rotation damper and a 14-bit AS5048B Magentic Rotary Encoder (parts B and D) to measure rotation angle from the straight-facing position. This sensor measures handle rotation angle continuously and feeds this information back to an Arduino Mega 2560 and mounted new Bluetooth Low Energy (BLE) Shield by RedBear.

The rotation damper design for the handle mount support is illustrated in Figure 2. The silicon 'X'-shaped insert fits tightly between two plastic female parts (parts C and F) that experience relative rotation. Part E holds the unit together and restricts deformation of the silicon into part F. Part D glues to part F to hold the magnet component on the sensor stationary. The silicon is compressed during rotation against parts F and C to prevent excessive displacement angles of the handlebars that may occur with large force imbalances.

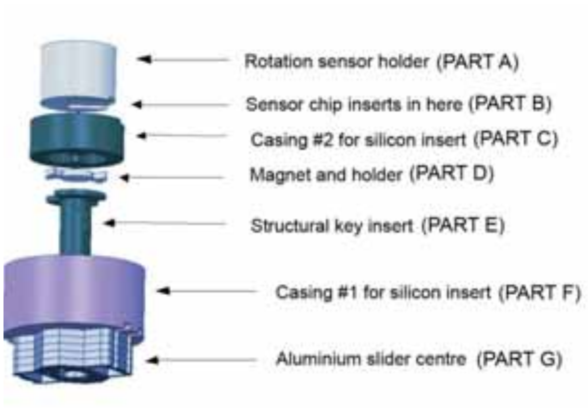


Figure 2. Z-axis rotation mechanism with silicon damper

## Communications Structure

The communication structure for the ReachHab is shown in the block diagram in Figure 3.

The iPad connects to the Arduino Mega Bluetooth Low Energy (BLE) Shield wirelessly using Bluetooth 4.0 protocol and a custom-written script with the app techBASIC. techBASIC is a software tool for collecting, analyzing, processing and displaying data using in-built mathematical graphing tools.

The monitoring system is programmed in BASIC, and allows data from the handle rotation angles to be displayed on the iPad screen as the sensor readings are intercepted. Once measured on the iPad, the data can be emailed directly to the appropriate physiotherapist at the end of each physiotherapy session for progress monitoring. Considering the target age group of 60-80 year olds, iPad icon buttons were designed to accomodate for psychomotor and visual deficiencies, as recommended by Caprani et al. [15]

Data is transmitted at a maximum rate of 19200 baud along BLE networks. Future testing should be conducted to assess whether this rate of data transmission, with processing time, produces a sufficiently fast mixed reality system to provide an engaging environment for neurorehabilitation of motor control.

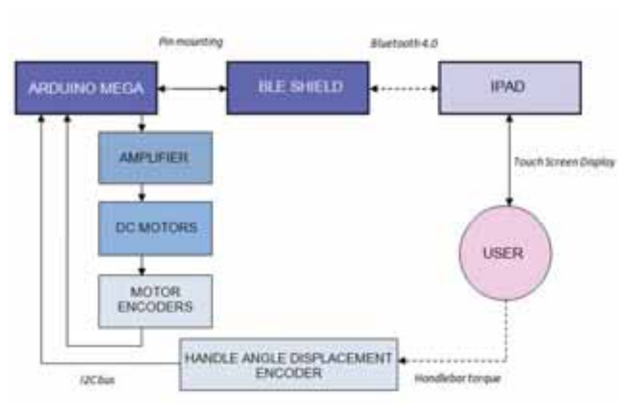


Figure 3. Electronic communications block diagram

At this initial project phase the interface system was simple to allow a proof of concept to be tested before complicated programmes and operational modes were developed.

## 2. Methods

By analysing joint angles at the thorax, shoulder, elbow and wrist when using the ReachHab and comparing resultant joint rotation angles and angular velocities to existing literature on characteristic reaching in healthy participants, it can be assessed whether the mechanical design of the ReachHab will teach its users to move correctly for rehabilitation.

Ethics approval for this research testing was granted by the University of Auckland Human Participants Ethics Committee on 28th August 2013 for a period of three years. One sixty-five year old female participated in this study conducted at the University of Auckland Biomechanics Laboratory. Signed declaration of informed consent was obtained from the participant prior to testing.

A work table was set up near the centre of the laboratory with the ReachHab positioned on top, facing a chair for the participant to sit in. The location of this chair was determined such that it would be approximately central to the view of the eight infrared Vicon MX cameras (Oxford Metrics Group, Oxford, UK) used to record the participant's motion when using the ReachHab.

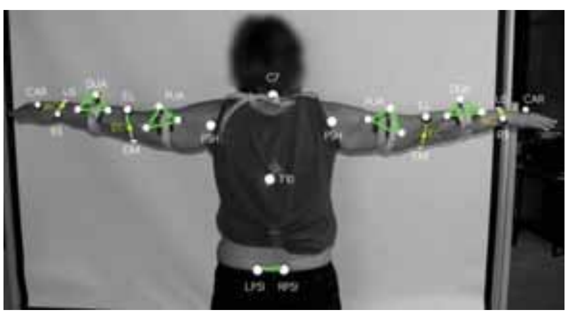

**Figure 4.** Passive reflective marker positioning on participant, from back

These cameras were set to record at a frequency of 100Hz. A digital camera was positioned to record the participant using the device in the sagittal plane.

Spherical passive reflective markers were attached to the participant at biomechanically relevant landmarks as shown in Figure 4. Table 1 details the marker label abbreviations and the exact anatomical locations of each marker on the body. The anatomical marker positioning model used by Zhang et al for an upper limb cricket bowling study in 2011 was used. [16] The Vicon system modelled the human body as a series of rigid body segments, connected by joints of various degrees of freedom. By registering the positions of the reflective markers, the Vicon system calculated the virtual locations of joint centres on the participant and positioned three-dimensional cartesian coordinate systems at each joint.

Five different ReachHab platform angles, α were tested by the participant: 5, 10, 13, 18, and 20° of elevation. The participant was asked to push the handlebars along the slider from a sitting position, to bring them to the top of the platform as feels comfortable before returning to original resting position at the base of the platform. Four trials of five cycle repetitions were performed for each platform angle, giving a total of 20 cycles at each platform angle. After each trial the participant was given the opportunity to rest briefly before the next trial began.

**Table 1.** Marker acronyms and their anatomical locations

| Marker | Position | Marker | Position |
|---|---|---|---|
| ASH | Anterior shoulder | PSH | Posterior shoulder |
| PUA | Upper-arm cluster | DUA | Forearm cluster |
| EM | Medial epicondyle | EL | Lateral epicondyle |
| RS | Radial styloid | US | Ulnar styloid |
| EC | Elbow centre | SC | Shoulder centre |
| C7 | 7th cervical vertebrae | CLAV | Clavicular notch |
| STRN | Sternum | T10 | 10th thoracic vertebrae |
| LASI | Left anterior superior iliac spine | RASI | Right anterior superior iliac spine |
| LPSI | Left posterior superior iliac spine | RPSI | Right posterior superior iliac spine |
| WC | Wrist centre | CAR | Metacarpal |

## Data Processing

The virtual coordinate systems calculated for each joint centre are shown on an anatomical model. Data was processed using the Vicon Workstation and Bodybuilder programmes (Oxford Metrics Group, Oxford, UK).

A moving-average filter was taken every 7 data points to smooth short-term fluctuations in data and highlight the longer term time trends in the participant's movement trajectories. Local segment coordinate systems were created for the thorax, upper arm, forearm, hand and pelvis segments based on marker positions. Axes in these right hand coordinate systems were defined according to the International Society of

Biomechanics. [17] The anatomical UL model from Zhang et al was altered slightly to remove unnecessary components for this study. The origin of the thorax was defined as the midpoint between the CLAV and C7. Once defined, the coordinates of each segment of the model were transformed with respect to its reference segment by a sequence of three rotations delineated by the three Euler angles outlined by Grood and Suntay. [18] The order was defined as flexion/extension, adduction/abduction, internal/external. The start of each cycle was taken as the time from initial departure of the handle section from the base of the ReachHab platform, before the handle was pushed to the top of the slider and then returned back to the base of the platform, at which point the cycle time stopped.

## 3. Results

The shoulder flexion angular velocity curve over one cycle at 20° is shown in Figure 5 against Kamper et al's healthy arm velocity profile for performing a reach motion in 16 chronic stroke patients. [19]

The full-reach point (the zero velocity point at mid-cycle) times and end-times were similar between Kamper's participants and the ReachHab participant.

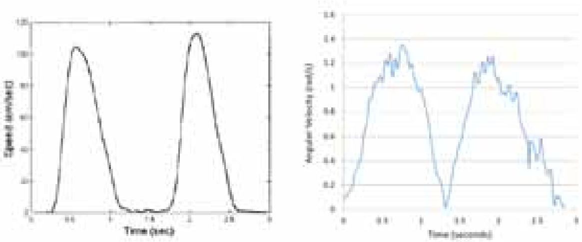

**Figure 5.** Velocity curve profiles from reaching in literature (left) and with the ReachHab (right)

Figures 6 and 7 show the shoulder and elbow angles normalised over one cycle at the maximum tested platform angle of 20°. The mean cycle time at a platform angle of 20° was 2.9 seconds. Anterior shoulder flexion in Figure 6 smoothly ranged between 0° and 60°, while anterior elbow flexion had a range of almost 100° rotation over a single cycle. Lateral shoulder movement during the reach was shown with shoulder adduction to peak at a mean angle of -28° at the same time as the shoulder flexes to its peak angle of 60°. Internal shoulder rotation was highly variable.
The thorax flexion/extension angle range was only 5° of rotation for the participant.

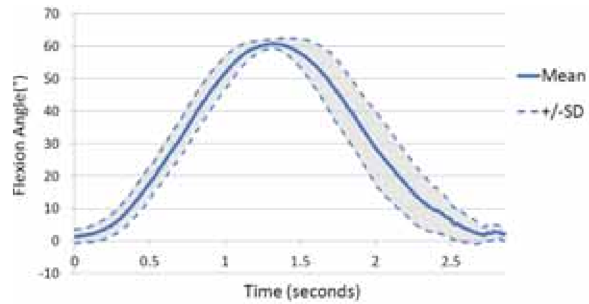


**Figure 6.** Shoulder flexion angles normalised over one cycle at a platform angle of 20°

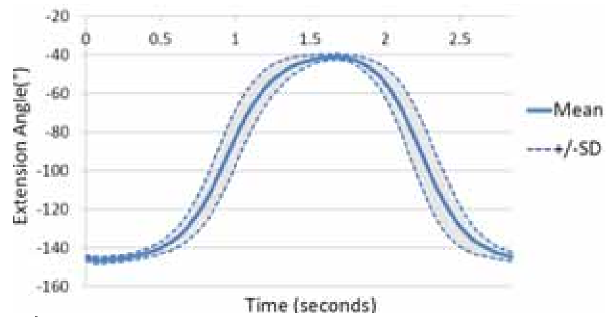


**Figure 7.** Elbow extension angles normalised over one cycle at an angle of 20°

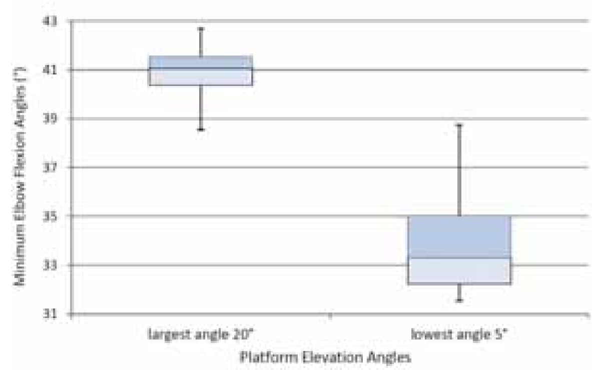


**Figure 8.** Minimum elbow flexion angles at two different ReachHab elevation angles

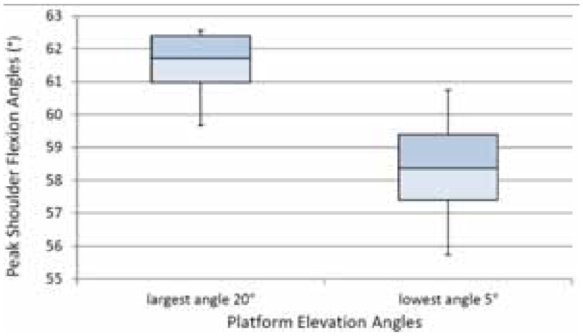


Figure 9. Peak shoulder flexion angles at two different ReachHab elevation angles

Comparing between the greatest and smallest platform angles shows lower peak flexion angles at both the wrist and shoulder for a shallower platform, as seen in Figures 8 and 9. The median elbow flexion peak angle differed by almost 8°, when comparing between a 5 degree and a 20° platform angle, whilst the peak shoulder flexion angle differed by only around 3°.

## 4. Discussion

The shoulder flexion angular velocity curve over one cycle at 20° approximated the dual bell-curve shape of Kamper et al's healthy arm velocity profile for performing a reach motion in 16 chronic stroke patients. Shoulder flexion peaked at an average of 1.3 seconds through the 2.86 second cycle with the ReachHab participant. Shoulder adduction and wrist radial deviation all peaked in synch with the main shoulder flexion movement at the 1.3 second mark, illustrating kinematic coupling between these movements. The elbow flexion angle peaked around 0.3 seconds later, reflecting the typical reaching kinematics expected, where the primary movement is initially dominated by shoulder flexion before being pushed further by additional elbow extension.

The larger standard deviation in shoulder flexion and adduction in the return phase of the reaching cycle illustrates a higher variability when moving the arms down back to the ReachHab starting position. It can be expected that this larger variability reflects instability in the user's handle control and larger handle rotations in the return phase. It may therefore be desirable to alter the monitoring system to distinguish between the upwards extension and return phases of reach, to assess more clearly where in the cycle the user is experiencing the largest difference in UL ability. This will provide an indication to physiotherapists on which movements are the most difficult and thus where to focus complementary therapy.

Thorax flexion/ extension was negligible. However, since excessive trunk flexion/ extension is a common compensatory measure for UL spasticity in stroke patients, stroke patients using the ReachHab will likely experience increased flexion angles when using the ReachHab. [20] The smooth shoulder and elbow curves closely approximate literature for characteristic reaching kinematics. [19-21] Lower peak flexion angles at both the elbow and shoulder for a shallower platform were noticed compared to a steeper platform. This supports the theory that lower platform angles should be used in more severe cases of hemiplegia to avoid shoulder pain associated with increased shoulder flexion or any excessive stretching in spastic muscles. [22]

Considerably more rotation was observed around the z-axis rotation damper mechanical design for the net torque applied than was desired. This implies that a stiffer material 'X'-shaped damper insert should be used to reduce the rotation movement and produce the +\-10° rotation desired for the sizes of bilateral force output imbalance we are expecting to see. Despite the expectation that testing the ReachHab with a healthy participant would result in no handle rotation, small fluctuations in angles were subjectively observed.

Although this device encourages a characteristic reaching motion in healthy participants, compensatory bilateral reaching strategies observed in stroke patients such as increased trunk flexion and abnormal shoulder to elbow moment coupling means the possibility exists that the same motion may not be achieved in stroke patients. [20] While a full clinical trial involving multiple hemiparetic MAS level 4 and above stroke participants and age-matched controls would confirm whether the ReachHab improves functional reaching ability in the targeted population, preliminary results indicate a successful proof of concept and provide evidence in support of further development.

## 5. Conclusions

- Shoulder and elbow flexion joint angles, thorax flexion and kinematic coupling between the shoulder and wrist with the ReachHab closely approximate previous studies on natural reaching kinematics
- Increasing platform elevation angle increases the required elbow extension more than it increases shoulder flexion
- The ReachHab silicon rotation damper for measuring UL force disparity is insufficiently stiff for the expected UL impairment of the target patient group
- The ReachHab has been successfully proven in concept and shows strong potential for improving UL reaching rehabilitation after stroke

## Acknowledgements

Thank you to Professor Shane Xie and Dr Andrew McDaid for their guidance and supervision, and well as Dr T Claire Davies for her continued support.

Thanks also to Heather Gordon and the staff at the Laura Fergusson Rehabilitation Centre, Logan Stuart for suggestions on the basic structure of the x-y slider design, and to Dr. Yanxin Zhang for the generous use of the Biomechanics Laboratory at the University of Auckland.

## References

[1]. J. Mackay, G. Mensah, Global Burden of Stroke, *World Health Organisation.* (2013)

[2]. V. Feigin, C. Lawes, Stroke epidemiology: a review of population-based studies of incidence, prevalence, and case-fatality in the late 20th century, *The Lancet Neurology.* (2003) *2*, 43-53

[3]. Liu, Waller, Kepple, Whitall, Compensatory arm reaching strategies after stroke: Induced position analysis, *Journal of Rehabilitation Research and Development.* (2013) *50*, 71-84

[4]. Pelton, van Vliet, Hollands. Interventions for improving coordination of reach to grasp following stroke: a systematic review, *International Journal of Evidence-Based Healthcare.* (2012) 89-102

[5]. J. Whitall, & S. Waller, Bilateral arm training: Why and who benefits? *NeuroRehabilitation,* (2008) *23*, 29-41

[6]. Wu Ching-yi et al. Effect of Therapist-Based Versus Robot-Assisted Bilateral Arm Training on Motor Control, Functional Performance, and Quality of Life After Stroke: A Clinical Trial, *Physical Therapy.* (2012), *92*

[7]. S. Masiero, A. Celia, G. Rosati, M. Armani. Robotic-Assisted Rehabilitation of the Upper Limb After Acute Stroke, *Archives of Physical Medicine and Rehabilitation* (2007) *88*, 142-149.

[8]. N. Foley, R. Teasell, J. Jutai, S. Bhogal, E. Kruger. Upper Extremity Interventions. *The Evidence-Based Review of Stroke Rehabilitation (EBRSR),* (2012).

[9]. I. Howard, J. Ingram, D. Wolpert. Context-Dependent Partitioning of Motor Learning in Bimanual Movements, *Journal of Neurophysiology.* (2010) *104*, 2082-91

[10]. J. Cauraugh, N. Lodha, S. Naik, J. Summers. Bilateral Movement Training and Stroke Motor Recovery Progress: A Structured Review and Meta-Analysis, *Journal of Neurological Sciences,* (2006) *244*, 89-95

[11]. K. Stewart; J. Cauraugh, J. Summers. Bilateral movement training and stroke rehabilitation: A systematic review and meta-analysis, *Journal of the Neurological Sciences* (2006) *244*, 89-95

[12]. A. VanDelden, C. Peper. A Systematic Review of Bilateral Upper Limb Training Devices for Poststroke Rehabilitation. *Stroke Research and Treatment.* (2012) *2012*, 1-17

[13]. S. Pheasant, C. Haslegrave. Bodyspace: Anthropometry, Ergonomics, and the Design of Work, *Taylor & Francis/CRC Press* (2006)

[14]. J. Stewart, S. Cramer. Patient-Reported Measures Provide Unique Insights into Motor Function After Stroke, *Stroke.* (2013) *44*, 1111-1116

[15]. N. Caprani, N. O'Connor, G. Gurrin, F. Cheein. Touch Screens for the Older User. *Assistive Technologies.* (2012)

[16]. Y. Zhang, J. Unka, G. Liu. Contributions of joint rotations to ball release speed during cricket bowling: A three-dimensional kinematic analysis. *Journal of Sports Sciences.* (2011)

[17]. G. Wu, et al. ISB recommendation on definition of joint coordinate systems of various joint for the reporting of human joint motion - Part II; shoulder, elbow, wrist and hand. *Journal of Biomechanics,* (2005) *38*, 981-992

[18]. E. Grood, W. Suntay. A joint coordinate system for the clinical description of three dimensional motions: application to the knee, *Journal of Biomechanical Engineering,* (1983) *105*, 136-144.

[19]. D. Kamper, A. McKenna-Cole, L. Kahn, D. Reinkensmeyer. Alterations in reaching after stroke and their relation to movement direction and impairment severity. *Archives of Physical Medicine and Rehabilitation.* ( 2003) *82*, 702 – 707.

[20]. Liu, Waller, Kepple, Whitall. Compensatory arm reaching strategies after stroke: Induced position analysis, *Journal of*

*Rehabilitation Research and Development. (*2013*) 50*, 71-84
[21]. M. Cirstea, M. Levin. Compensatory strategies for reaching in stroke,*Brain. (*2000*) 123*, 940-953
[22] I. Lindgren, A. Jonsson, B. Norrving, A. Lindgren. Shoulder pain after stroke, *Stroke. (*2007*) 38*, 343-348

# Implementation of Self-Sensing Air Muscles in a Hand Robot

N. Yip, D. Hariharan
The University of Auckland,
Department of Mechanical Engineering,
Mechatronics Engineering,
New Zealand

**Abstract:**
This article outlines the design and construction of a 'self-sensing pneumatic air muscle' (SSPAM) and the robotic hand used to demonstrate its use. Pneumatic air muscles are compliant, non-linear actuators which are currently controlled by bulky, rigid position sensors. A novel flexible position sensor was integrated into a pneumatic air muscle to form a SSPAM. These SSPAMs were characterised by comparing measurements from a laser rangefinder and the integrated sensor. The sensors responded to the change in radial expansion and tracked the contraction of the SSPAM well with an average gauge factor of -2.23. To demonstrate the use of SSPAMs, a robotic hand was designed and constructed with nine degrees of freedom. The SSPAMs were connected to the finger joints using strings to close the joints and springs were used antagonistically to open and re-extend them. The hand was controlled using a program written in NI LabView to operate each joint.

**Keywords:** Air muscles, flexible position sensor, PID controller

## 1. Introduction

The air muscle is a pneumatic actuator developed by McKibben in the 1950's [1]. It is widely implemented in anthropomorphic robotic applications because of its force compliance and similarities to the human skeletal muscle. A rubber tube makes up the core of the structure, with nylon cross hatch woven mesh surrounding the core. Both ends of the rubber tube are sealed and an inlet port for compressed air is inserted into one end. As shown in Figure 1; the air muscle is initially held extended by a spring. When compressed air is passed into the inlet pipe; the rubber core expands radially. Since the outer weave is inextensible, this results in an axial contraction that is proportional to the air pressure[2].

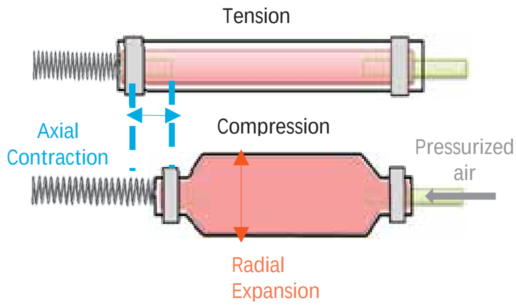


Figure 1. Schematic view of air muscle in tension and compression

Because air muscles behave non-linearly, a sensor is required to monitor the contraction to attain accurate control of its position. Most sensors used for this purpose have traditional mechanical designs and are rigid and bulky, in contrast to the flexible air muscles. Therefore, in recent years, a lot of research has been focused on integrating a sensor inside the air muscle to provide a compact "all-in-one" implementation of the actuator and sensor. However the non-conventional sensors developed so far were ineffective because they were either obtrusive, had non-linear behaviour or were too hard and impractical to manufacture [3-5].

A flexible position sensor was developed by PhD student, Arief Tjahyono, at the University of

Auckland in 2012. The sensor's small size, light weight and flexibility provided the opportunity to explore its integration inside an air muscle [3].

## Project Goals

The goals of this project were to:

- Design and construct a self-sensing pneumatic air muscle (SSPAM),
- Characterise the behaviour of a SSPAM, and
- Demonstrate the use of SSPAMs in a robotic hand.

## 2. Flexible Position Sensor

The sensor was made using a thin strip of natural rubber as the substrate with a thin film of the conductive polymer, polypyrrole (PPy), on its top surface. PPy is a conductive polymer; when the sensor is strained, its resistance increases linearly to the amount of strain applied.

The fabrication procedure consists of four main steps. First the natural rubber substrate is cut into 2 mm x 50 mm strips and pre-strained by 20% using a custom-made stretching rig. Next, the loaded stretching rig is placed into the March CS-1701 RIE machine to treat the top surfaces of the rubber strips with oxygen plasma at 200 W for 40 seconds. After this, the top surfaces of the rubber strips, still loaded in the stretching rig, are immersed in a solution of 0.5M $FeCl_3$ in acetonitrile for two hours. The plasma treatment increases the surface hydrophilicity of the rubber and makes it more absorbent to the $FeCl_3$. After the $FeCl_3$ solution, the rig is placed in a vacuum at -0.9 bar with 1mL of 0.1M pyrrole solution in acetonitrile. At -0.9 bar the pyrrole solution vaporises. Polymerisation occurs when the vaporised pyrrole reacts with the $FeCl_3$ on the surface of the rubber strips.

Once fabricated, the sensors were tested by straining them in 2 mm increments and measuring the resistance reading using an ohm meter. The resistance and position of the sensors were normalised and the gauge factor calculated using Equation 1.

$$Guage\ Factor = \frac{Change\ in\ Resistance}{Change\ in\ Length} = \frac{\Delta R/R_o}{\Delta L/L_o} \quad (1)$$

The values were normalised because the sensors have a characteristic upward drift in resistance overtime. The results gathered for one sensor is plotted in Figure 2.

As shown in Figure 2, the normalised change in resistance for each sensor was linearly related to the amount of strain applied. It was found that straining the sensors above 50% caused surface micro cracks to form on the PPy coating and damaged the sensors [3]. On average the gauge factor for the sensors was found to be 1.75.

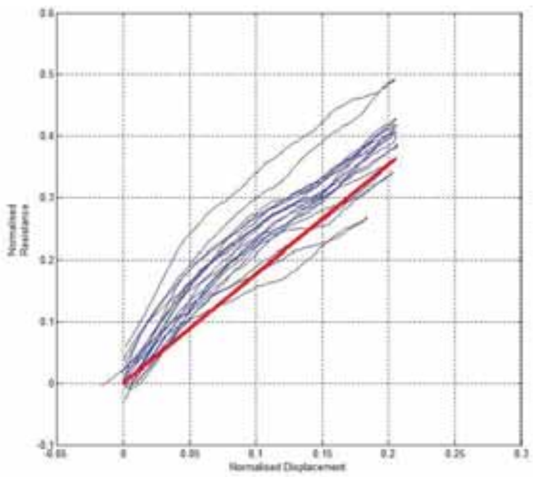

Figure 2. Plot of normalised resistance vs. normalised displacement of a flexible position sensor

## 3. Self-sensing Air Muscle

### 3.1. Design and Construction

Figure 3 depicts the schematic placement of the integrated sensor inside the air muscle. As shown, when pressurised air is passed into the inlet pipe; the air muscle contracts, pushing the sensor outwards, putting strain on the sensor and causing the resistance of the sensor to change.

PPy Flexible sensor

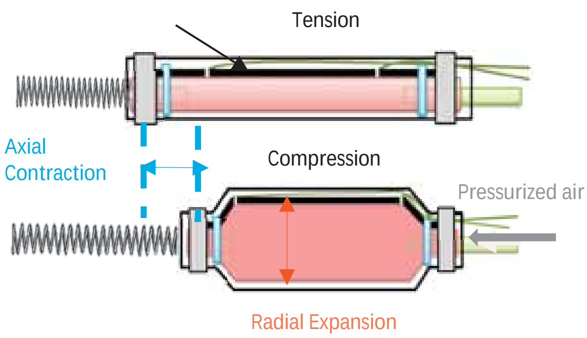


Figure 3. Schematic view of SSPAM in tension and compression

The sensor was secured to the rubber tube with zip ties such that it was stretched by 3 mm when the air muscle was in its non-extended state, with the polymer coating facing towards the mesh. Pre-straining the sensor in this manner ensured the sensor never go slack regardless of the state the SSPAM was in.

The nylon sheath was bunched up such that it only allowed the air muscle to extend up to a maximum of 10mm in its fully contracted state. This meant that the sensor was stretched to a maximum of 25% (13 mm maximum displacement) of its initial length. Consequently, the maximum strain the sensor was subjected to was well below the 50% limit and this safeguarded the sensor from damage. A fully constructed SSPAM is shown in figure 4. In its extended state, the SSPAM had a length of 120 mm and a width of 10 mm.

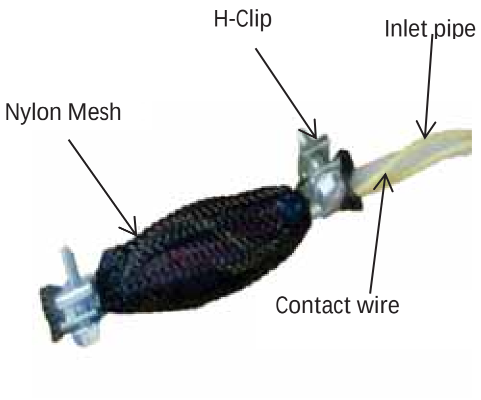


Figure 4. Fully constructed SSPAM

## 3.2. Characterisation

The SSPAMs were first tested to ensure integrating the sensor did not have any negative effect on the air muscle's operation. This was done by comparing the force and stiffness characteristics of the air muscle with and without a sensor integrated. It was found that in both cases the results were similar and therefore the sensor was capable of operating unobtrusively.

The following sections detail the experimental procedure undertaken to characterise the self-sensing capability of the SSPAMs.

### 3.2.1. Sensor performance test rig

The test setup used for measuring the sensing capability of the integrated sensor is depicted in Figure 5.

The user interacts with the characterisation rig via a LabView® user interface running on a PC. A National Instrument PCIe-6321 data acquisition (DAQ) card and SCB-68 board was used to transfer data between the PC and the characterisation rig. The program outputted a voltage signal through the DAQ card to an SMC ITV0030-3BS electro-pneumatic valve. The valve regulated the internal air pressure supplied to the SSPAM based on the input voltage signal. The valve had an input voltage range of 0 to 8V which corresponded to a pressure of 0.1 to 4bar.

A compression spring was fitted parallel to the SSPAM on the testing device. When the internal pressure of the SSPAM increased, the SSPAM contracted and the slider was pulled. When the internal pressure was decreased, the SSPAM relaxed and the compression spring provided the antagonistic pushing force to re-extend the rig and SSPAM.

As shown in Figure 5, a Banner L-GAGE LG10A65PU laser rangefinder was used to measure the absolute position of the air muscle. The laser rangefinder was calibrated at the fully extended and fully contracted positions of the air muscle (corresponding to an internal pressure of 0.1 bar to 4 bar). The laser's readings were used to provide the reference point to compare the integrated sensor's performance.

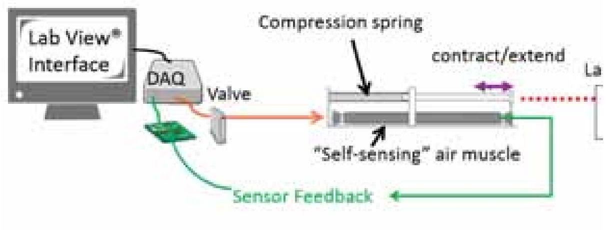


Figure 5. Arrangement of test setup to measure the integrated sensor performance

### 3.2.2. Characterisation Software

A PID controller was implemented in Lab View® to regulate position control. A Butterworth filter was used in the program to eliminate the electrical noise from the FP sensor and provide an accurate signal to the PID controller. Because the electrical noise form the sensor's output signal consists of high frequency components, the Butterworth filter was set to behave as a low pass filter with a 20 Hz cut off frequency [3].

The control loop implemented is illustrated in Figure 6; *r(t)* is the set point input, *e(t)* is the position error, u(t) is the input voltage to the valve that controls the air pressure of the air muscle and *y(t)* is the contraction of the air muscle. As shown in the figure, either the integrated sensor or the laser rangefinder could be included in the feedback loop as an alternative sensor. The performance of the sensor was assessed by using the Laser rangefinder's measurements as feedback to the PID controller. The integrated sensor's reading was compared to that of the laser rangefinder by plotting the measurement on Excel [3].

The set points for the control test were set starting at 48 mm and decreased to 42 mm, in 2 mm step sizes. These set points were set in a sequential manner to analyse the accuracy of the integrated sensor. A hold time of 30 seconds was set for each set point to provide information on the integrated sensor's stability and the effect of its drift in resistance over time.

The user interface allows the user to input values for G and C; they relate the normalised change in sensor resistance to the displacement of the air muscle using Equation 2. C corresponds to the starting position of 48 mm. The inverse of G corresponds to the gauge factor of the SSPAM. The G value was manipulated to find a value which provided a response that best followed the laser reading.

$$Contraction\ displacement = G(\Delta Resistance) + C \qquad (2)$$

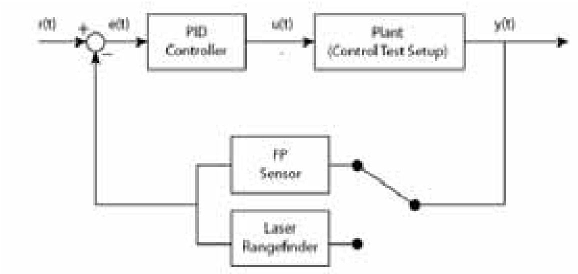


**Figure 6.** Control loop for position control test with the integrated sensor as feedback to the PID controller and the Laser sensor as alternative feedback [3]

### 3.3. Results and Analysis

For this sensor, a G value of -0.4 was found to provide a response that most closely tracked the set point. For this case, the maximum difference in reading of the integrated FP sensor compared to the laser rangefinder was 1.03 mm. The integrated FP sensor had a small upward spike every time the set point changed. The graph also depicts an offset between the integrated FP sensor and the set point at the end of the position control step sequence. The G value is negative as an axial contraction in the air muscle corresponded to an increase in the resistance of the integrated sensor.

On average, the gauge factor of the SSPAMs was found to -2.23.

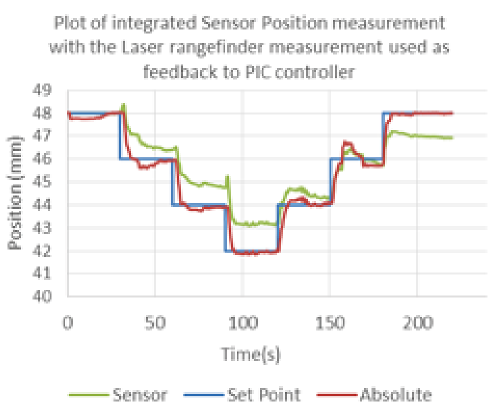


Figure 7. Response from sensor performance test setup of PID controller with integrated sensor and using the laser sensor measuring absolute position as the feedback

## 4. Implementation

To demonstrate the advantages of using the SSPAMs, a robotic hand was designed and constructed. The robotic hand was designed to be as similar as possible to an average human hand and had a total of nine controlled degrees of freedom, two for each finger and one for the thumb.

### 4.1. Design

The design of the robotic hand was divided into three parts, the fingers to be actuated, actuation mechanism where the SSPAMs were used and the supporting structures to connect the fingers and actuation mechanisms.

#### 4.1.1. Finger Design

The fingers were dimensioned according to the average corresponding bone lengths as measured in a study of 66 adults conducted by A. Buryanov and V. Kotiuk[6]. The average thickness of a human finger is an uncommon unit of measure known as finger breadth, which corresponds to 20 mm. This thickness was used for the middle finger, the ring and pinkie fingers were slightly thinner and the index and thumb slightly thicker.

#### 4.1.2. Actuation Mechanism Design

SSPAMs are thicker than 20 mm when they contract so they could not be used to control the finger joints directly. Instead they were used to pull strings which were guided such that when they were pulled they would close the finger joint that they controlled. As shown in Figure 8, the blue line shows the path of the string used to close the middle-proximal joint and the red line shows the path of the string used to close the proximal-metacarpal joint.

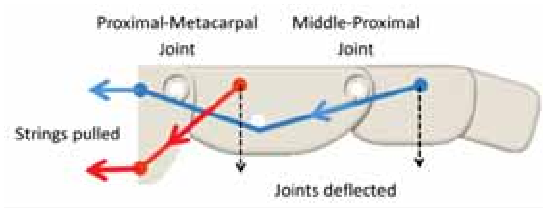


Figure 8. Finger actuation diagram

Due to the SSPAMs being unidirectional actuators, tension springs were used antagonistically to return them to their extended (relaxed) state. The string controlling a finger joint was attached in between the tension spring and SSPAM so the contraction of the SSPAM would pull the finger joint closed. A torsion spring was attached to each finger joint to provide the return force to open again when released by the SSPAM. A schematic for the finger actuation mechanism described is shown in Figure 9.


Figure 9. Actuation mechanism schematic

#### 4.1.3. Kinematic Analysis

A kinematic analysis was conducted to relate the contraction of the SSPAMs in the actuation mechanism to the angle of deflection of the finger joint it controlled. It was assumed that the change in length of the SSPAM would propagate through the string connecting the two, and result in an equivalent change in length of the red line labelled $L_a$ in Figure 10. With this assumption, the models for each of the two different joint mechanisms, previously described in Figure 8, were similar and therefore the same series of calculations were applied to both.

The model shown in Figure 10 was used to calculate joint deflection, $\beta$, from the contraction of the SSPAM using Equation 3. The positions of the string connection points were then used to convert $\beta$ into the deflection of the finger from its fully open position labelled $\alpha$ and $\gamma$ in Figure 11 using Equation 4 and 5.

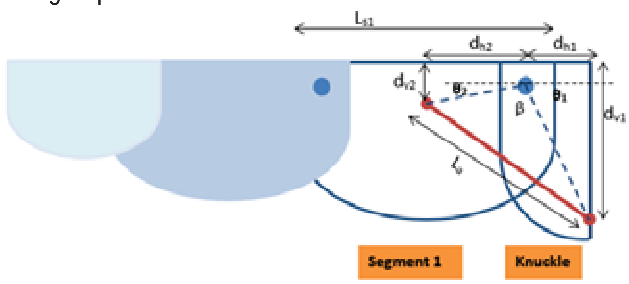


Figure 10. Kinematic analysis model

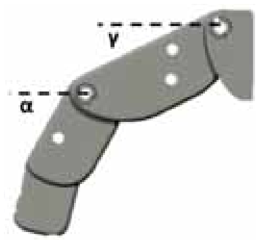

Figure 11 Finger deflection diagram

$$\beta = \cos^{-1}\left(\frac{{d_1}^2+{d_2}^2-{L_a}^2}{2d_1d_2}\right) \tag{3}$$

$$\alpha = \pi - (\theta_1 + \theta_2 + \beta) \tag{4}$$

$$\gamma = \pi - (\theta_1 + \theta_2 + \beta) \tag{5}$$

### 4.1.4. Supporting Structure Design

The palm and forearm for the robotic arm were dimensioned to be similar to an average adult's hand. The length was calculated with reference to a study conducted by A. Agnihotri, *et al.* [7] and the widths of our own hands. According to these dimensions the palm was designed to hold four SSPAM actuation mechanisms and the forearm was designed to hold the remaining five. The four mechanisms to be mounted in the palm were to actuate the four middle-proximal joints on each of the four fingers. The five mechanisms to be mounted in the forearm were to actuate the five proximal-metacarpal joints (including the one in the thumb).

As shown in Figure 12, the robotic hand was constructed and three SSPAM mechanisms were implemented to control the two joints in the index finger and the one joint in the thumb.

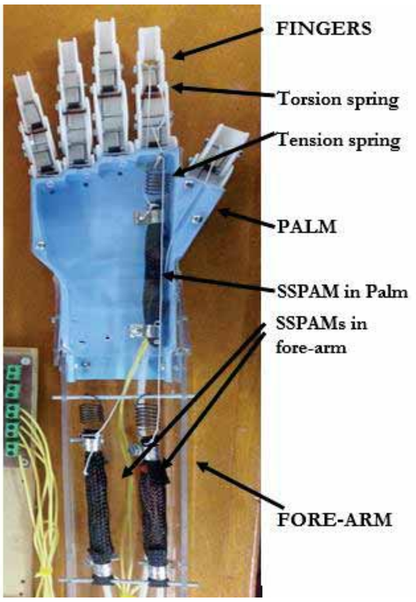


Figure 12. Fully assembled robotic hand

## 4.2. Control

The controller for the robotic hand was developed in the NI LabView® environment. A NI SCB-68 board (connected to a DAQ board) was used to connect the signals from the robotic hand to the controller running in the Ni LabView environment on a PC.

### 4.2.1. Hardware

The hardware used to interface the SSPAMs in the robotic hand, to the computer, is shown in red in Figure 13. The change in resistance from the integrated sensor is converted to a change in voltage and then amplified and read by the DAQ.

To interface the computer to the air muscles in the hand, the blue line in Figure 13 shows the controller outputs a digital control voltage through the DAQ. This is converted to an analogue voltage and then input to an electro-pneumatic valve. This is used to regulate the internal pressure of a single air muscle. Each valve takes an input voltage between zero and 8V and regulates the pressure in the air muscle between 0.1 and 4bar.

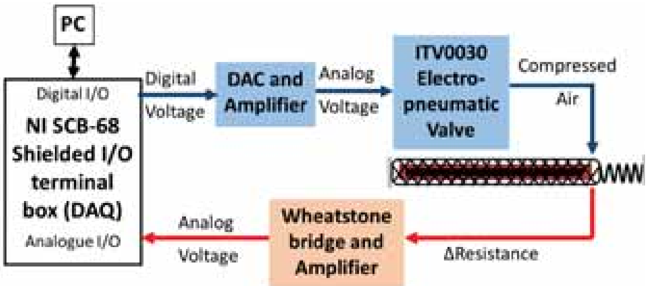


Figure 13. Hardware control loop

### 4.2.2. Software

The controller was run on a PC and read its inputs and outputs from the DAQ. The controller flow diagram is shown in Figure 14. The initial resistances for each of the sensors in the SSPAMs were recorded in order to compensate for the drift in resistance over time. As long as the initial resistance was known, the gauge factor of a SSPAM could be used to calculate its change in length.

A PID controller was used to control the SSPAMs because the feedback from the integrated sensor was shown to be linear as explained in Section 2. A discrete PID controller was implemented as it calculated the control output one iteration at a time. This allowed the controller to loop through each SSPAM in the hand by remembering and setting the correct PID values for each.

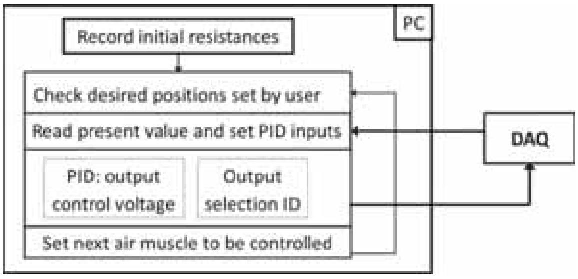


Figure 14. Software controller loop

A user interface was used to set the desired positions for each of the finger joints in the robotic hand.

As shown in Figure 15, the control constants were first set and then either of two modes of control could be selected. The automatic mode allowed a choice of pre-programmed hand positions (open or closed). In manual mode, each joint could be controlled independently (either open, half closed or fully closed).

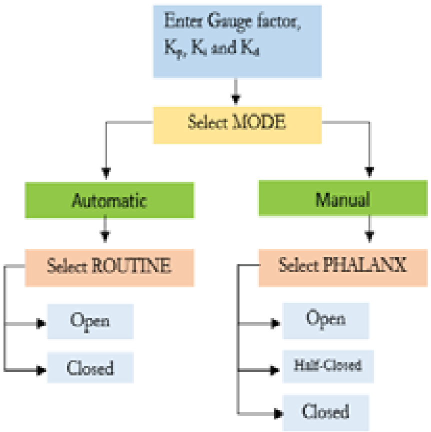


Figure 15. User interface flow diagram

### 4.3. Results and Discussion

The kinematic analysis revealed that a 10 mm contraction of the SSPAM would lead to a range of motion of approximately half the range of motion that a human finger can exhibit. The summary of the theoretical range of motion calculated from a 10mm contraction for each of the joints analysed is shown in Table 1.

The SSPAMs were limited to contracting by 10mm due to the equipment available for the sensor fabrication limiting the length of the integrated flexible position sensors which could be produced. Longer flexible position sensors could be integrated into longer SSPAMs and therefore a contraction of more than 10mm could be achieved.

The actual range of motion for the two joints on the index finger and the thumb was measured on the robotic hand. It was noted that the range of motion achieved by the hand was about 60% of the theoretical ranges of motion calculated. The string experienced some friction which reduced the change in length of the air muscle seen by the finger, reducing the actual joint range of motion.

Table 1. Comparison of the measured joint range of motion of the robotic hand

| | Human | Theoretical | Measured |
|---|---|---|---|
| Index Middle Phalanx | $100^{0}$ | $53^{0}$ | $35.1^{0}$ |
| Index Proximal Phalanx | $105^{0}$ | $50.6^{0}$ | $47.2^{0}$ |
| Thumb Proximal Phalanx | $80^{0}$ | $54.7^{0}$ | $26^{0}$ |

## 5. Conclusions

The proposed flexible position sensor was successfully integrated with a pneumatic air muscle and the resulting SSPAM was fully designed and constructed. The SSPAM had an average negative gauge factor of 2.23 and the use of a SSPAM was successfully demonstrated by the design and implementation of a hand robot.

## Acknowledgements

We would like to thank: Dr Kean Aw for his invaluable support and supervision; Logan Stuart and Ken Snow for their technical help in constructing the SSPAMs and the robotic hand; Robert Pitt, for his time spent designing and manufacturing the springs for the robotic hand; Bryon Wright for the use of the cleanroom for fabricating the flexible position sensors; and Young Ho Choe, for teaching us how to make the flexible position sensors.

## References

[1]. Sugisaka, M. *An approach for soft humanoid robot with artificial muscles*. in *Industrial Electronics,*

*2009. ISIE 2009. IEEE International Symposium on*. 2009.

[2]. Ku, K.a.B., R.S. and Lam, K. and Yeung, L.F. and Li, R., *A Novel Actuator for Underwater Robots*. Oceanic Engineering, 2009. 34: p. 331-342.

[3]. Tjahyono, A.P., *Development of a Novel Flexible Position Sensor for the Control of Hand Exoskeletons*, in *Mechanical/ Mechatronics Enigneering*2012, University of Auckland: Auckland, NewZealand.

[4]. Yeung, D.P.T., *Investigation Of Danfoss Polypower Deap As An Alternative Large Strain Sensor*, 2012, The University of Auckland.

[5]. Dohta, S., *et al*. *Development of String Type Flexible Displacement Sensor to Measure the Movement of Robot and Human Body*. in *Mechatronics and Machine Vision in Practice, 2008. M2VIP 2008. 15th International Conference on*. 2008.

[6].Buryanov, A., and Kotiuk, V. (2010). *Proporciones de los Segmentos de la Mano (Proportions of Hand Segments)*. International Journal of Morphology, 28(3), pp. 755–758.

[7].Agnihotri, A., Purwar, B., Jeebun, N., and Agnihotri, S. (2006). *Determination of sex by hand dimensions*. The Internet Journal of Forensic Science, 1(2), pp. 12–24.

# Evaluation of IPMC and PVDF as Wearable Energy Harvesters

J. Park, F. Dong
The University of Auckland,
Department of Mechanical Engineering,
Mechatronics Engineering,
New Zealand

## Abstract:

This article entails the characterization and comparison of the power outputs of Ionic Polymer-Metal Composite (IPMC) and Polyvinylidene Fluoride (PVDF) when mechanically bent at the elbow joint during walking and running. Using two equally sized strips of IPMC and PVDF, the comparison was made fair and representative by using volume as a baseline reference. Methods were also looked into for enhancing the natural power outputs seen from the materials. The aim of this project was to settle claims suggesting IPMC is a good energy harvester and to optimize the power output. Conclusions from our research showed that PVDF is a much better energy harvester than IPMC, and that the power output from PVDF can be greatly increased by creating a PVDF bimorph with rubber. With a maximum output of 3.54 μW from two PVDF bimorph strips in parallel, great potential was seen for trickle charging of a small capacitor.

Keywords: IPMC, PVDF, Energy harvesters, Transduction

## 1. Introduction

With the vast increase in interest towards powering all deployed sensor networks and mobile electronics, there has been a simultaneous increase in interest in the ability to power these devices without the use of a battery. This is due to the short economic life span of batteries and their frequent need for replacement. Energy harvesters are a solution to this problem. They are designed to harvest energy from their surrounding environment in a form desired by the user.

This project focused on the two human motions most naturally seen in life – walking and running; and their ability to harvest electrical energy from the mechanical energy produced at the elbow joint, during these gaits. It involved two materials for comparison: Ionic Polymer-Metal Composite (IPMC) and Polyvinylidene fluoride (PVDF).

Both IPMC and PVDF have been proven in previous studies [1, 2] to be possible options for mechanical to electrical energy harvesting applications. Often lacking however was the comparison between the two materials. This project aimed to fill this void of knowledge in addition to maximizing the power output.

## 2. IPMC versus PVDF

Simulations were undertaken to compare the power outputs of both IPMC and PVDF using a short strip of each with dimensions of 28 mm (*l*) × 7 mm (*w*) × 0.2 mm (*t*). This involved bending the materials at various bending angles with respect to a fixed bending rate, and varying the bending rates with respect to a fixed bending angle.

Considering arm movement frequencies typically seen during walking and running are 0.9 Hz and 1.083 Hz, and the angle of rotations are typically 30° and 25° respectively [3], the bending rates for each gait was found to be 54°/s and 54.15°/s. Therefore, simulations were taken for bending angles between 20° and 80° and bending rates between 27°/s and 189°/s. These produced the following results as shown in Figure 1 and 2.

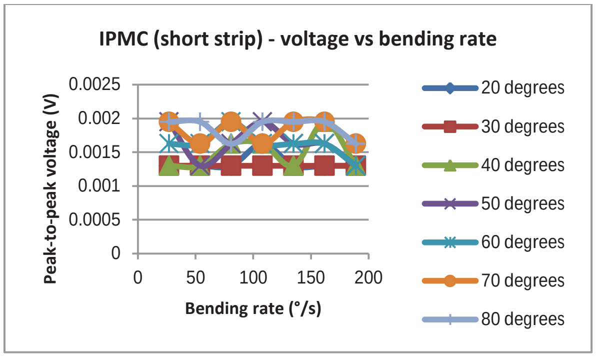


**Figure 1.** IPMC Peak-to-peak voltage vs. bending rate graph

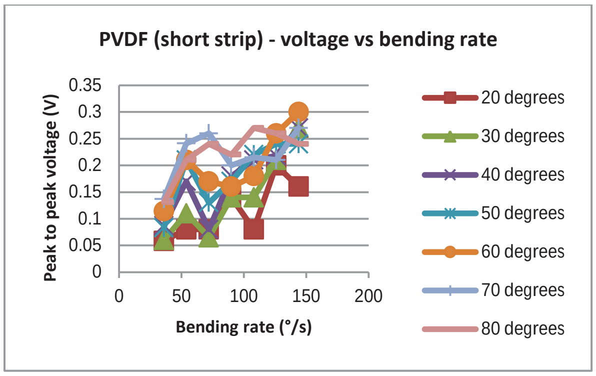


**Figure 2.** PVDF Peak-to-peak voltage vs bending rate graph

These graphs show the highest peak-to-peak voltage for IPMC was 1.95 mV and the highest peak-to-peak voltage for PVDF was 300 mV. In addition, using the formula:

$$Power_{max} = \frac{Voltage^2}{Resistance}$$

in conjunction with the optimum load resistances (270kΩ and 1950kΩ for IPMC and PVDF respectively), the maximum power produced by IPMC was 14.08pW, and the maximum power produced by PVDF was 45nW. With an absolute power produced that was orders of magnitude greater than the power from IPMC, it was clear that the PVDF strip was a better energy harvester than IPMC. Therefore all remaining experiments were only done with PVDF.

While this analysis would have been significant for a typical energy harvesting characterization, for use in our application, it was only the relevant data that matched our applications parameters that were important. Therefore, for use in a human energy harvester, where the bending rate of a human limb joint is approximately 54 °/s for both walking and running, it was the power produced in these scenarios that were relevant. It can be seen that both gaits produced similar results, and from the graphs, it was seen that under these conditions, the highest peak-to-peak voltage for IPMC was 1.3 mV and for PVDF was ~110 mV. Furthermore, they show that with the consideration of respective load resistances, the highest power generated from each was:

$$\text{IPMC:}\quad Power_{max} = \frac{0.0013^2}{270000} = 6.26\ \text{pW}$$

$$\text{PVDF:}\quad Power_{max} = \frac{0.11^2}{2{,}000{,}000} = 6.05\ \text{nW}$$

While the voltages for the IPMC graph showed no particular trend as the bending rate and bending angle was increased – other than remaining stable, it was clear that for PVDF, the peak-to-peak voltages were higher when the angle of rotation was increased, and when the bending rate was increased. This was as to be expected for the PVDF due to the increase in stress caused from the increase in bending angle, and the increase in rate of change of stress caused by the increased in bending rate.

## 3. Short strip PVDF vs Long strip PVDF

After determining that PVDF was better than IPMC, it was realized that a larger piece would be needed to better accommodate the large radius of curvature seen in elbows (~5cm). It was also hypothesized that using a larger surface area would increase the power output. Therefore a longer strip of PVDF of size 7cm (*l*) × 8mm (*w*) × 0.2mm (*t*) was characterized and a comparison of the the results with the characterisation of a short strip is shown in Figure 3.

Note that here, and in all following plots, an arbitrary step frequency of 50 Hz and a bending angle of 30.6° were used.

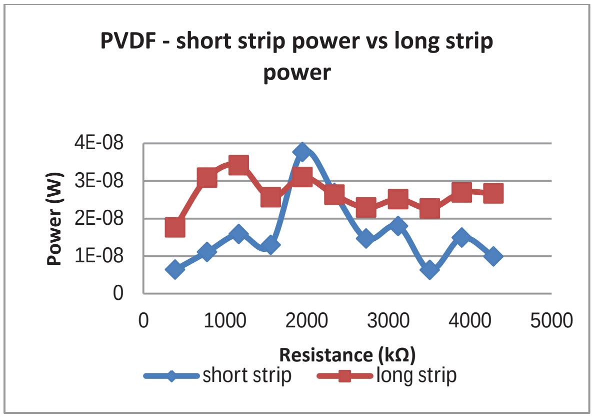


Figure 3. Comparison of the output power from a short strip of PVDF and a long strip of PVDF

This graph shows that while a long strip generally produced a higher power output than the short strip, the increase in power was not directly proportional to the 2.6 factor increase in area.

## 4. Long strip Characterisations

With the power output still too low for use, to increase the power output, combinations of multiple long strips of PVDF were tested with the results as shown in Figure 4.

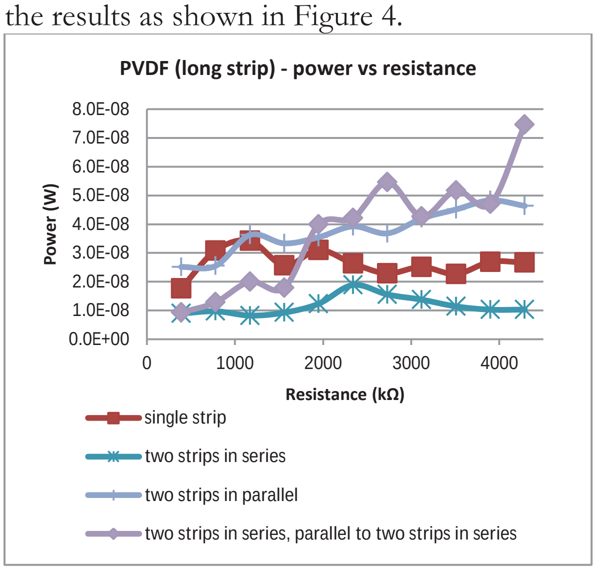


Figure 4. Comparison of different arrangements of long strips of PVDF

This shows that having two strips of PVDF in series slightly reduced the power output from a single strip and having two strips of PVDF in parallel increased the power output (by approximately two times). It can also be seen that having two strips in series or parallel to another two strips in series, reduced the power output at resistances less than 1950kΩ, and increased the power above this resistance (by approximately 2.8 times). With the power output increased by a factor of 2.8 from a single strip, this arrangement appeared to work well. However, relative to two strips in parallel, this arrangement was deemed less efficient. This is because two strips in parallel increased the power output by a only factor of 1.74; and although this theoretically should have been 2, extrapolating from the real data showed that four strips in parallel would be more efficient than two strips in series or parallel to two in series, with a total increase factor of 3.48 comparable to 2.8.

Here it was also identified that while intuitively the PVDF energy harvester was thought to be resistive, should have been thought of as capacitive [4] and has to be taken into consideration when impedance matched.

## 5. Bimorph structure

The piezoelectric formula for sensor applications states that:

$$V = (d_{31} * \sigma_1 * t_{piezo})/\varepsilon$$

where $t_{piezo}$ is the material thickness (m)
$\varepsilon$ is the electrical permittivity (F/m)
$d_{31}$ is the piezoelectric strain coefficient for our 31 mode PVDF (C/N)
$\sigma_1$ is the mechanical stress in the 1-direction (N/m$^2$).

Using this equation, it was identified that while the $d_{31}$, $t_{piezo}$ and $\varepsilon$ were fixed material properties, the $\sigma_1$ could be increased to increase the voltage output. Therefore to increase this parameter, a brief test was conducted by bending short strips of PVDF glued on to other materials with lower flexibility, in the form of a bimorph, in an attempt to increase the stress in the 1-direction. (Short strips were used over longer

ones to conserve the limited material that was provided at the start of the project).
Using a load resistance of 3900 kΩ, a plot of the results from the different methods tested is shown in Figure 5.

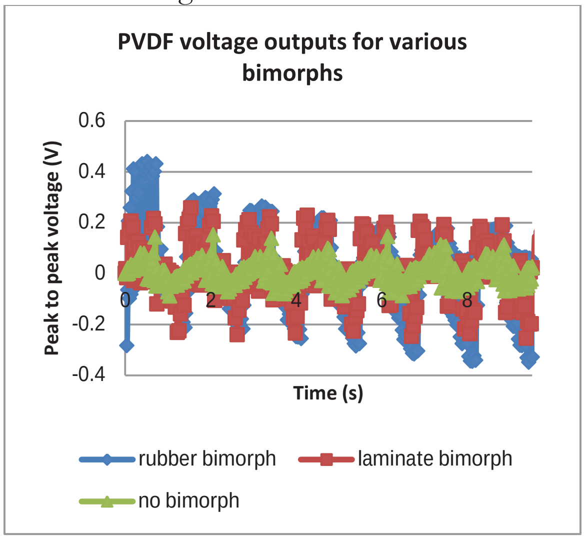


Figure 5. Comparison of PVDF voltage outputs for no bimorph, laminate bimorph, and rubber bimorph

From this, it was evaluated that rubber bimorphs increase the voltage output the most, and hence all remaining tests were done with PVDF in a bimorph with rubber.

## 6. Simulated Voltage Harvested

From the following equation [4]

$$V_c = \frac{d_{31} Y_c b_c}{C_p} \int_0^{L_c} \epsilon_1 dx$$

where $\epsilon_1$ is the strain in the 1 directions
$C_p \propto I_c B_c$ and $S_q \propto I_c B_c$
$I_c$ is the width and
$B_c$ is the length of the strip of PVDF
it can be seen that there needs to be an integrating factor across the length of the strip in order to obtain the voltage that can be harvested. However, since the PVDF is approximated as an isotropic material, the voltage can be obtained similarly by integrating the stress across the length of the PVDF strip and then dividing by the length of the strip. To approximate this, the result obtained by a finite element analysis was averaged across all nodes within the model and the result of the averaged stresses is shown in Table 1.

Table 1. Averaged stress across strips

| Bimorph | Averaged Stress (\|Pa\|) |
|---|---|
| Thin aluminium plates only | $0.48\times10^6$ |
| Thin aluminium plates and rubber | $0.67\times10^6$ |

Processing this data we can show that the theoretical voltages that can be harvested across the strips during an open circuit are as shown in Table 2.

Table 2. Simulated voltage across strips

| Bimorph | Voltage (V) |
|---|---|
| Thin aluminium plates only | 44.5 |
| Thin aluminium plates and rubber | 62.3 |

## 7. Bimorph vs Non-Bimorph

Following the findings in the previous two sections, more elaborate tests were done using long strips of PVDF of size 7 cm (*l*) × 1.2 cm (*w*) × 0.15 cm (*t*) in a rubber bimorph of size 7.5 cm (*l*) × 1.2 cm (*w*) × 0.15 cm (*t*). This involved characterizing combinations of multiple strips of rubber bimorph PVDF and analysing the results. An image of the strip is shown in Figure 6 and a plot of the data is show in Figure 7.

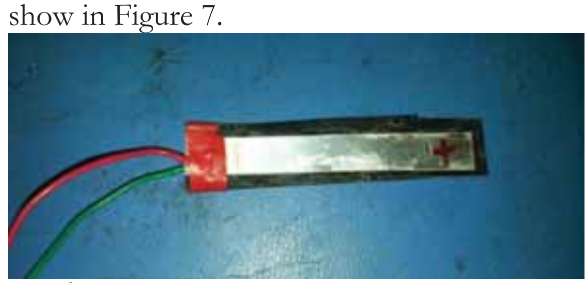

Figure 6. Long strip of rubber bimorph PVDF

Note that the two copper wires (red and green) under the red tape were for use as inputs.

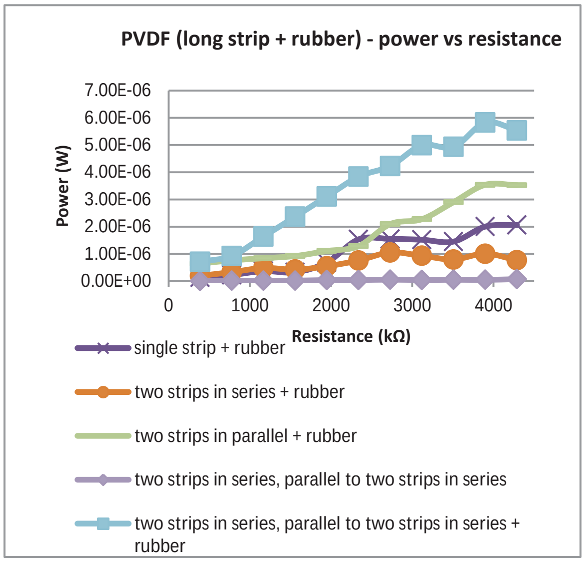


Figure 7. Comparison of different arrangements of long strips of PVDF with a rubber bimorph

Note this graph (PVDF/rubber bimorph) includes points from the combination that produced the highest power output without rubber (i.e. two strips in series, parallel to two strips in series) as a reference to highlight the magnitude of voltage increased from rubber bimorph.
This graph also shows that the general trends remain similar with the trends identified without rubber, with the exception that more power is generated with this bimorph.
Comparing this graph with Figure 4, it can be seen that with rubber/PVDF bimorph:

- A single strip increased the power output by a factor of 74
- Two strips in series increased the power output by a factor of 70
- Two strips in parallel increased the power output by a factor of 78
- Two strips in series, parallel to two strips in series (i.e. 4 strips) increased the power output by factor of 117

This showed that having this bimorph always improved the power output by at least a factor of 70. It also showed that while for the combinations involving two strips or less, the increase factor was ~74, the increase factor for two strips in series, parallel to two strips in series was 117, implying a relative increase factor of 1.58. This conferred extremely well with the findings in section 4 where the increase factor from a parallel connection to the connection with two strips in series, parallel to two strips in series, was 1.61.
With a load resistance of 3900 kΩ, while theoretically it was expected that the voltage output be 62.3 V, experimentally, only a peak voltage of 2.97 V was achieved from a long strip of PVDF with rubber bimorph. The theorized increase factor for power output for a single strip of PVDF with rubber, compared to without rubber was also greatly mismatched with a factor of 1.96 compared to 74.

These large margins of error were likely due to the following factors:

- Inaccurate initial $d_{31}$ value
- Abaqus has overestimated the stress, due to inadequate information
- The model used in Abaqus is not a perfect representation of our scenario
- The epoxy used was likely not to transfer all the stress from the rubber to the PVDF.

Following these results, all remaining experiments were done with two rubber long strips of PVDF with rubber bimorph connected in parallel.

## 8. Bridge Rectifier and capacitor

After characterizing the power outputs from the PVDF and load circuits, the power was attempted to be further increased by using a bridge rectifier to rectify the voltage into a unipolar signal, and a capacitor to store the charge.

Results obtained from bending two rubber bimorph PVDF strips in parallel (i.e. the most efficient power output combination) are plotted as shown in Figure 8.

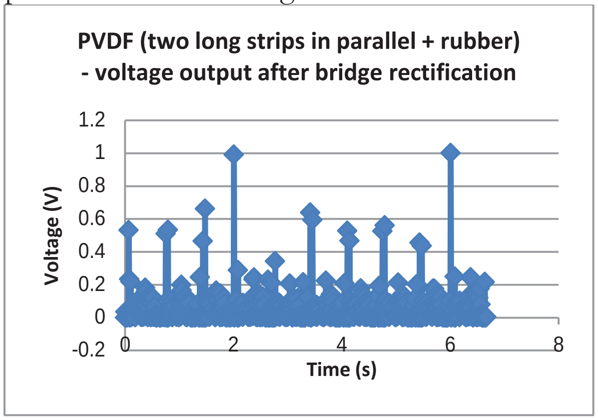


Figure 8. Output from a bridge rectifier circuit

This shows a clearly rectified signal with a peak voltage of 1V. Due to this being an infrequent spike however, it was preferable to use a more frequent value for calculations. Therefore, it was decided that the effective peak voltage which could be obtained with stability, was 0.53V.

The lowest power Schottky diode available was the BAT754S. With a forward voltage of 260 mV and a forward current of 1 mA, the total power required to drive this diode was 0.26 mW [5]. With an extremely low forward resistance of 260 Ω, this was relatively much lower than the load resistance of 3900 kΩ and was hence considered negligible.

Compared to the peak voltage obtained from the parallel combination of long strips of rubber bimorph PVDF, i.e. 3.72 V, it was clear that significant power was being used to overcome the forward bias of two diodes.

Attempting to store charge on a capacitor, the bridge rectified output was connected to various load capacitors with the results as shown in Figure 9.

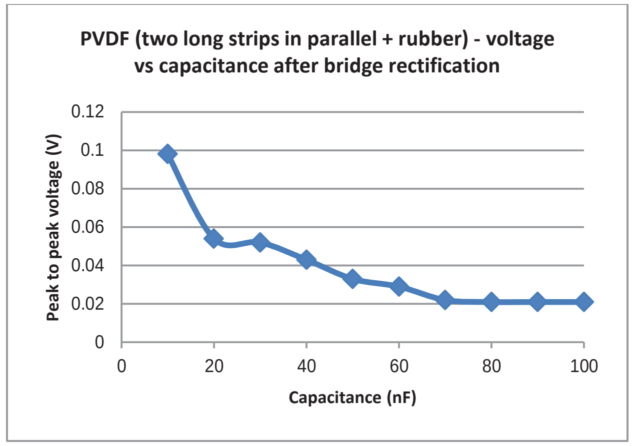


Figure 9. Output from a bridge rectifier circuit with capacitive load

While adding the capacitor did smooth out the voltages, it was clear that they were not efficient enough, and that the output from the PVDF was not frequent enough to store enough charge to be of use in an immediate application. It was also seen that from the bridge to resistive load, the voltages dropped by a factor of 5.41, from 0.53V to 0.098V with a capacitive load. The PVDF with different capacitive loads without rectification is shown in figure 10.

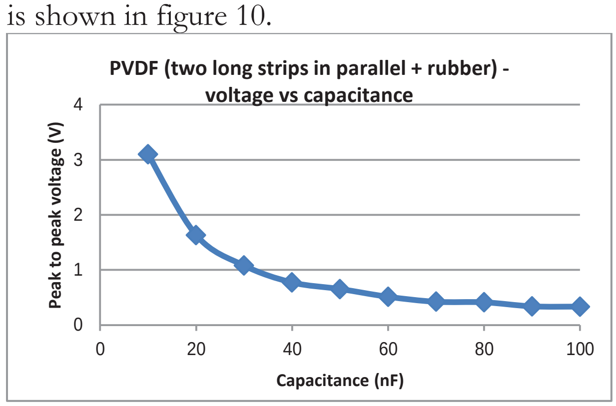


Figure 10. Peak to peak voltage obtained when the load was measured across a capacitor without rectification circuit

This showed that with an increase in load capacitance, the peak to peak voltage across the load reduced. These results were as to be expected due to the limited charge that can be produced from the PVDF.

## 9. Conclusions

- PVDF produces more power than IPMC
- The highest and most efficient peak-to-peak power generated by PVDF occurs when a long strip of PVDF is in a bimorph with rubber, and two of these strips are connected in parallel. This produces up to 3.5 μW
- The power produced by PVDF exhibited good potential to be used for trickle charging a small battery or a super capacitor


## Acknowledgements

We would like to thank the following people for their tremendous efforts, support and time:

Assoc. Prof. Kean Aw – Project Supervisor; without whom this project would not have been possible.

Harold Tarun – First Semester Mechatronics Lab technician; handled our part orders and helped solder some tough surface mounted pieces.

Logan Stuart – Second Semester Mechatronics Lab technician; produced our PCB's, ordered required parts and offered useful tips.

Ken Snow – Second Semester Manufacturing lab technician; allowed access to the manufacturing laboratory, and their 3D printers.


## References


[1]. Fourie, D., Shoe-Mounted PVDF Piezoelectric Transducer for Energy Harvesting Texas A&M University. p. 1-4.

[2]. J Brufau-Penella, M.P.-V., P Giannone, S Graziani and S Strazzeri, Characterization of the harvesting capabilities of an ionic polymer metal composite device. 2008: p. 1-15.

[3]. E.Yu Shapkova, A.V.T., and M.L. Latash, Arm motion coupling during locomotion-like actions: An experimental study and a dynamic model. 2011.

[4]. Chopra, J.S.a.I., Fundamental Understanding of Piezoelectric Strain Sensors. 2001, University of Maryland. p. 248 - 253.

[5]. NXP, BAT754S series. 2003. p. 2-4.

# Development of an Autonomous Quadrotor for Aerial Manipulation

Akash Arora, Young Ho Choe
The University of Auckland,
Department of Mechanical Engineering,
Mechatronics Engineering,
New Zealand

## Abstract:

Aerial manipulation is a relatively new area of research, where an unmanned aerial vehicle is used to physically interact with the environment through the use of a gripper or manipulator arm. In this project, an ArduCopter quadrotor was used to develop an aerial manipulation system that could perform the task of autonomously grasping an object from the ground. A modular design for the quadrotor was developed, consisting of four main components which made up the entire autonomous system. These modules were the gripper system, the object detection system, the altitude controller and position controller. Apart from the position controller, each of the individual modules worked quite well. The altitude controller allowed the quadrotor to hold its altitude at specified heights with a maximum error of 25cm, while the object detection system was able to find the position of an object relative to the quadrotor with an average error of 0.16cm. The gripper system allowed the quadrotor to grasp objects of up to 800 of mass.

**Keywords:** Unmanned Aerial Vehicle, IR camera, gripper, control

## 1. Introduction

Unmanned Aerial Vehicles (UAVs) have gained immense popularity from both hobbyists and research groups in the last ten years.

A quadrotor is an aerial vehicle which utilises four propellers for flight. By changing the rotational speed of the propellers the quadrotor can ascend, descend and rotate in all three axes.

Quadrotors and UAVs in general have traditionally only been used passive applications such as surveillance and reconnaissance. A new and exciting area of research is in the field of aerial manipulation. This is where the quadrotor physically interacts with the environment via use of a gripper or a manipulator. Possible applications for this may be object retrieval, transportation of light loads in disaster situations, sample collecting in dangerous areas, or drop-off of equipment in a dangerous environment. The aim of this project was to develop an inexpensive quadrotor which could autonomously fly to an object and grasp it.

## 2. Part selection

To save time and ensure a good level of hardware performance, a decision was made to purchase a quadrotor kit. After extensive research, the Arducopter was chosen as the ideal starting platform. It was chosen due to its high payload capacity, customisability in hardware and software, low cost, flight stability and availability of online documentation. The kit contained an Arduino based open source flight controller and a frame constructed out of aluminium and fibreglass. Additional components such as a telemetry kit to allow real time data visualisation on a laptop, battery alarm and radio transmitter/receiver to allow manual control of the quadrotor.

## 3. Gripper design

In order to achieve the aerial manipulation task of object grasping, a suitable gripper had to be designed and implemented on the quadrotor. The design requirements that were identified for the gripper are listed below:

1. Light weight – because of the limited payload capacity of quadrotors, the gripper has to be as light as possible.
2. Versatile – the gripper should be able to grasp a wide variety of shapes and objects, instead of being designed for a specific type of object.
3. Good gripping strength – The gripper should be able to grip objects with masses of 500-1000g which is the typical payload capacity of the ArduCopter.
4. Wide – The gripper should have a relatively large gripping area so that it can grasp objects with a certain degree of uncertainty in the object's position. Having a small gripper would require more positioning effort when trying to pick up the object.
5. Long – The gripper should be long enough so that there is enough distance between the object being grasped and the quadrotor itself.

A 1-DOF gripper consisting of two claws coupled together with gears was designed on CAD. This design was chosen for its simplicity and its ability to fulfil all of the requirements set out above. The gears were 3D printed using high resolution printer while the arms were machined using polycarbonate. The gripper was designed so that it could be attached to the bottom centre of the quadrotor. Attaching the gripper in this position ensured that the centre of gravity of the quadrotor remained at the centre of the frame and didn't affect its flight stability.

**Figure 1.** CAD model of gripper

The gripper claws can fold up, and thus, the gripper does not hit the ground when the quadrotor has landed (Figure 1).

A servo motor was used to actuate the gripper due to its simple control and high torque to weight ratio. Calculations were carried out to ensure the servo can exert enough torque to grasp 800g.

The servo motor and the gripper proved to be very effective as it had the ability to grip a wide variety of objects and weights. Figure 2 shows the strength and versatility of the gripper. It had the ability to grasp objects as small as a pencil and grasp objects as large as a volley ball. The gripper also had the strength to grasp a full 750ml water bottle, weighing roughly 760g.

Figure 2. The gripper in action

## 4. Object Detection

A suitable object detection system needed to be implemented to allow the quadrotor to detect an object that it wishes to pick up, and calculate its relative distance to the quadrotor.
The Wii-remote is the main controller for the popular Nintendo Wii gaming console. The remote is capable of sensing the motion of the user through the use of an infra-red camera and on-board accelerometers and gyroscopes. The infra-red camera in particular has many desirable features that can be used in this project such as:

- Low cost- a Nintendo Wii remote can be purchased for $35
- Small size and weight- the camera measures 8x8x5 mm and weighs less than a gram.
- Uses I2C communication which is compatible with the flight controller.
- Has a built-in processor which carries out basic image processing. The camera simply outputs the x and y pixel co-ordinates of the four brightest infra-red blobs in the image.

By marking the object to be grasped by IR LEDs, a very low cost and reliable object detection system can be achieved.

Interface circuitry

To interface the camera with the flight controller some circuitry was needed. This includes a 25MHz oscillators, pull-up resistors and power and ground connections.

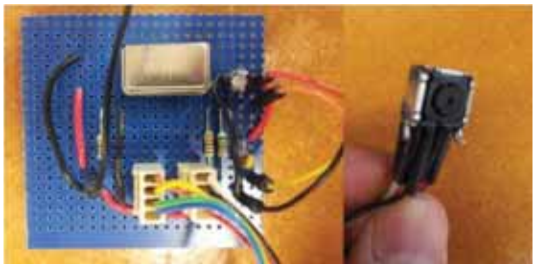

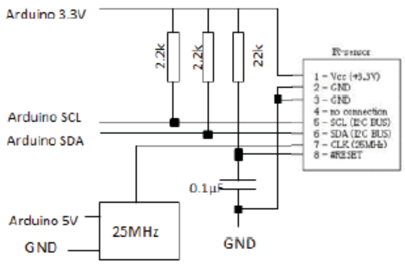


**Figure 3.** IR camera interface circuitry

Calculating position

As the quadrotor rolls and pitches, the orientation of the camera also changes. Mathematical relationships were derived to transform the image co-ordinates into metric position of the object.

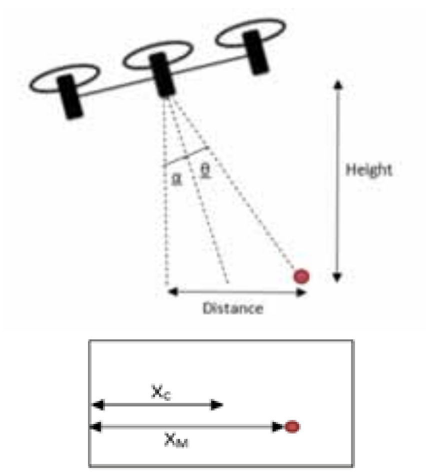


$$\theta = \frac{X_M - X_C}{\text{Pixels per degree}} = \frac{X_M - X_C}{24.0}$$

$$\text{Distance} = \text{Height} \times \tan(\theta + \alpha)$$

The validity of the equations was verified by carrying out an experiment. The camera was clamped at a fixed angle and an IR LED was moved. The position predicted by the camera and the actual position were compared. There was an average error of 1.6mm which shows that the equations accurately model the behaviour of the camera.

## 5. Altitude control

An altitude controller needed to be implemented to allow the quadrotor to accurately descend and ascend when attempting to grasp an object from the ground. An ultrasonic range finder was chosen to measure the quadrotor's height above the ground due to its low cost, good performance both indoors and outdoors, high noise rejection and being easy to use.

To improve the noise rejection of the sensor even further, a simple low pass filter using a resistor and a capacitor was added to the voltage line of the sensor. This helped reduce the high frequency spikes in the sensor's data. The ultrasonic sensor is powered by the APM flight control board and sends altitude information back to the board.

A PID controller was implemented to control the height of the quadrotor. It was found that the default control parameters did not give very accurate altitude hold. Therefore, the control parameters had to be manually tuned. However, even after tuning, the altitude controller was not able to hold the quadrotor's altitude at a specified height. The problem was identified as excessive vibrations in the quadrotor which caused the measured speed of the quadrotor from the APM board's IMU to be inaccurate. These vibrations were caused by the fast rotations of the motors and propellers. Therefore, in order to reduce these vibrations from affecting the IMU, the APM flight control board was mounted on top of vibration dampening gel (moon gel) as pictured in Figure 4.

Figure 5 shows the effect of the moon gel. The vibrations on the flight controller were measured by reading the accelerometer data in the z-axis during flight. It can be seen that without the moon gel the accelerations in the z-axis varied between $\pm 2m/s^2$. After applying the moon gel, the accelerations reduced dramatically so that it only varied between ±1m/s². This helped improve the performance of the altitude controller dramatically.

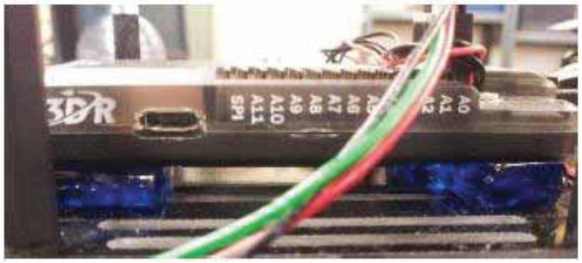


**Figure 4.** Moon gel mounted underneath the flight controller

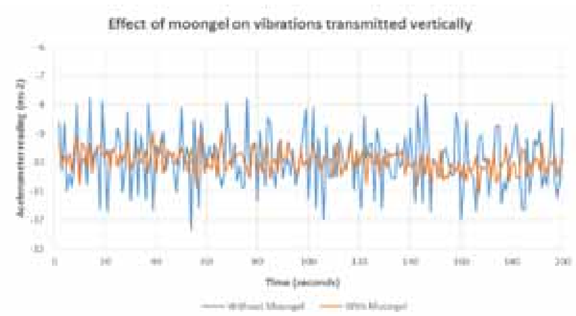


**Figure 5.** Effect of moon gel on transmitted vibrations

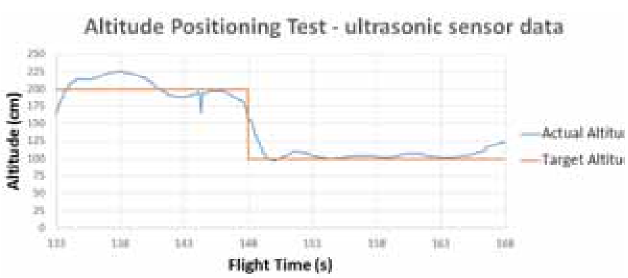


**Figure 6.** Altitude controller before and after tuning

A test was set up where the quadrotor was programmed to hold its altitude at 2m for 15 seconds and then descend and hold its altitude at 1m. Figure 6 shows the results of that test.
It can be seen that the quadrotor was able to follow the target altitude quite accurately. The maximum error in the altitude that can be seen is about 25cm. Most interestingly, there was no overshoot in the altitude when the quadrotor transitioned from 2m to 1m. This is very important for autonomous aerial gripping because if the quadrotor's altitude was to overshoot, it may hit the ground or the ceiling.

## 6. Position control

A position controller allows the quadrotor to position itself near the object in order to grasp it. An on-off controller was implemented to position the quadrotor above the object. The quadrotor rolls and pitches at fixed angles until it's within a 6cm square around the object. Unfortunately the quadrotor kept overshooting with this controller and was not able to remain still over the object.

## 7. Hardware overview

The fully assembled quadrotor is shown in Figure 8. The flight control circuitry is centrally located while the IR camera is placed underneath the quadrotor. The sonar sensor is at an offset from the centre to prevent interference from the gripper and the propellers.

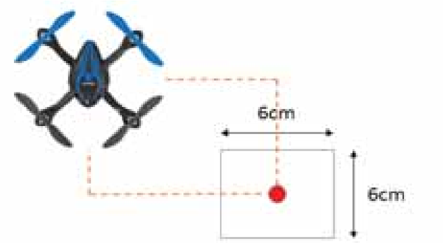


**Figure 7.** Position controller


**Figure 8.** Hardware overview

## 8. Conclusions

Moon gel was applied between the frame and flight controller. Vibrations were reduced by 50-75% in both horizontal and vertical directions and this improved the performance.

A 1DOF gripper was manufactured using 3D printing and polycarbonate which can grasp up to 800g.

An IR camera was able to predict the position of the object with an accuracy of 1.6mm.

An ultrasonic range sensor was used to control the height of the quadrotor with negligible overshoot.

An on-off controller was implemented to position the quadrotor above the object. More complex methods such as fuzzy logic or PIDs need to be trialled to improve position hold.

A Finite State Machine was designed, but not implemented, to co-ordinate all the different modules and allow fully autonomous flight.

## 9. Future works

Fuzzy logic should be attempted to achieve precise position hold above the object.

Implement a Finite State Machine to allow fully autonomous object grasping.

Design an adaptive flight controller which can take into account the change in the quadrotor's flight dynamics due to the added mass of the grasped object.

## Acknowledgements

Peter Xu- for his continued support and advice throughout the project

Ken Snow- for his help with manufacturing the gripper

Logan Anderson- for his assistance in soldering the IR camera

Sarath Pathirana- for promptly ordering parts

# Characterisation of Path Tracking Algorithms for GPS Guided Autonomous Vehicle

J.Y. Chia, M.C. Lee
The University of Auckland,
Department of Mechanical Engineering,
Mechatronics Engineering,
New Zealand

## Abstract:

One of the main characteristics of an autonomous ground vehicle (AGV) is the ability to determine its movement to achieve a desired path. Many different algorithms were developed to optimise the path tracking performance of an AGV. However, empirical testing on the algorithms is lacking, which has limited the understanding of the characteristics and performance of the algorithms on actual application. Hence, using the AGV platform developed at the University of Auckland, a series of tests were carried out to investigate two common path tracking algorithms, Follow-the-Carrot (FTC) and Pure Pursuit (PP) algorithms. The results show that FTC is able to perform sharper turns. FTC requires two control parameters to operate, which made it more difficult to tune, but offers better controllability. For PP, it mainly produces turns with large radius and has high tendency to produce overshoot around sharp corners. It requires only one control parameter, making it easier to tune but sacrificing controllability.

Keywords: Autonomous Ground Vehicle, Path Tracking, Follow-The-Carrot, Pure Pursuit

## 1. Introduction

An AGV is a mobile robot, which is capable of navigating through its environment without human control. The process of autonomous vehicle navigation can be divided into four basic steps which are: perceiving the environment, localizing itself within the environment, planning a path to its desired destination and executing the planned path. The Department of Mechanical Engineering at University of Auckland has been working on a Global Positioning System (GPS) Guided AGV since 2005, with the focus in localization and path tracking. In 2012, the AGV system displayed satisfactory path tracking capability using the FTC algorithm [1]. With such performance, the hardware and localization of the system were proven to be a sufficiently stable platform for different path tracking algorithms.

### Objectives

- Implement the Pure Pursuit and Follow-the-carrot algorithms into the AGV.
- Characterise Pure Pursuit and Follow-the-Carrot algorithms.

## 2. Platform Overview

This project was carried out on the AGV developed by the students of the University of Auckland, shown in Figure 1. The vehicle was built on an aluminium chassis [2]. The rear wheels are driven by drive motors while the front wheels are driven by a steering motor. The whole AGV is driven by a 14.8V Lithium Ion battery pack. Other than the GPS receiver, there are other sensors onboard to enhance the localization of the AGV, namely an Inertial Measurement Unit (IMU), a digital compass and two optical encoders. An ultrasonic sensor is employed to detect obstacle to prevent the AGV from colliding with obstacle.

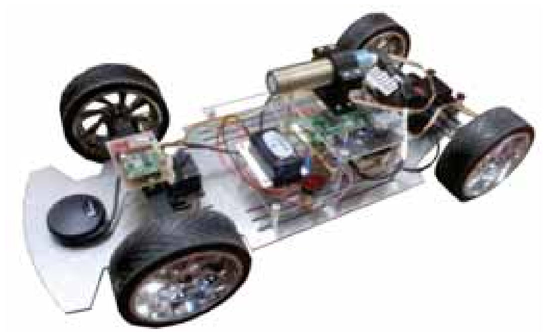

Figure 1. AGV platform.

The AGV is controlled by an AVR32 microcontroller by Atmel [1]. Using Bluetooth, user is able to send command to the microcontroller onboard through a Host PC Software on a laptop [3]. User is also able to collect data from the AGV during test runs.

Data are fed from the sensors to the microcontroller and fused using a 3-state Extended Kalman Filter (EKF) to obtain position of the vehicle. Using this information, turning radius is computed by the path tracking algorithm, which is then translated into pulse width modulation (PWM) signals to be sent to the servo motors. The overall system of the AGV is shown in Figure 2.

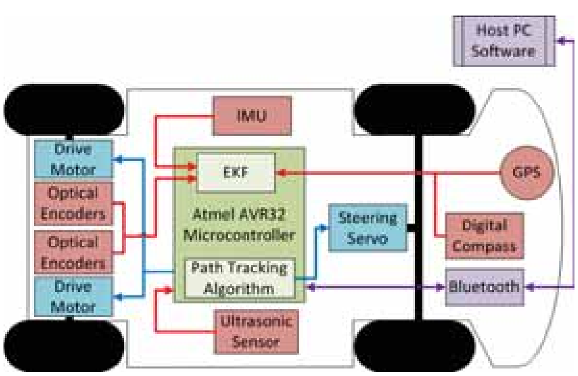


Figure 2. Overall system of AGV.

## Implementation

The path tracking module implemented in the AGV is broken down into four steps: defining path, locating Look Ahead Point (LAP), calculating the required turning radius and determining the vehicle steering angle.

<u>Define Path</u>

Firstly, the user is required to define the starting and ending points of the path in the local east, north, up (ENU) coordinate frame with metres as default unit. After that, path type is required to be defined, which can be either linear or circular. For circular paths, the radius of circle in metres and the path direction, which is either clockwise or anti-clockwise, has to be defined. Figure 3 illustrates two examples of the user defined paths.

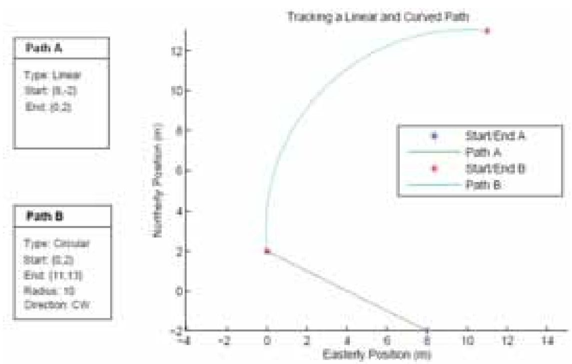


Figure 3. Examples for user defined path (Reproduced from [3])

<u>Locate Look Ahead Point</u>

The LAP is defined to be a temporary destination point located on the predetermined path which is one Look Ahead Distance (LAD) ahead of the orthogonal projection of the vehicle onto the path. For linear paths, the LAP can be calculated relatively easily and is illustrated in Figure 4.

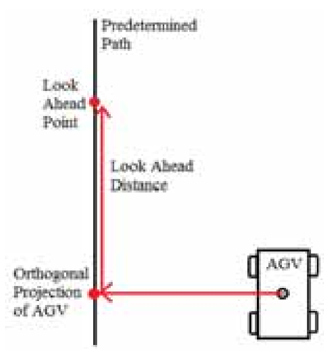


Figure 4. LAP calculation for linear path.

As for circular path, the LAP can be calculated through a series of steps and they are illustrated in Figure 5.

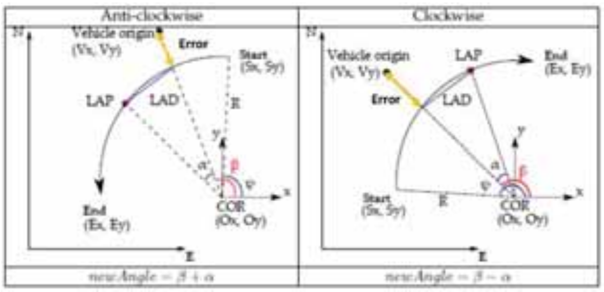


Figure 5. LAP calculation for circular path. (Reproduced from [1])

Calculate the Required Turning Radius

After finding the LAP, the vehicle calculates the turning radius necessary to reach the LAP, using either FTC or PP algorithms.

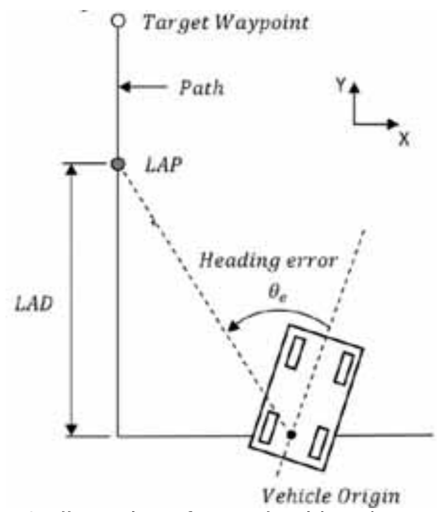


Figure 6. Illustration of FTC algorithm. (Reproduced from [2])

For FTC, the required turning radius, $r$, is calculated using orientation error, which is the angle between current vehicle heading and the straight line connecting the vehicle to the LAP, and a turning gain, K [4]. The calculation is illustrated in Figure 6 and shown in Equation 1.

$$r = \frac{1}{K\theta_e} \tag{1}$$

As for PP, the LAP is first converted into vehicle coordinate frame with vehicle at the origin. Then, an arc is constructed to join the vehicle to the LAP and is illustrated in Figure 7. With the arc, the turning radius can be calculated using Equation 2 [5].

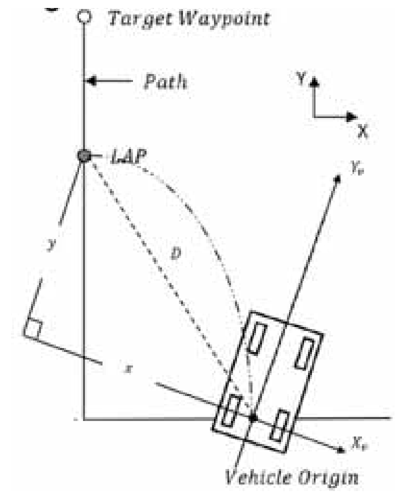


Figure 7. Illustration of PP algorithm. (Adapted from [2])

$$r = \frac{D^2}{2x} \tag{2}$$

Determine Steering Angle

The steering angle of the AGV can be calculated using Ackerman Steering Geometry. This geometry theory takes the turning radius, $R$, and the wheelbase, $L$, of the AGV to calculate the average steering angle, $\delta$, which is the average between the outer steering angle, $\delta_o$, and the inner steering angle, $\delta_i$. The steering angle calculation is illustrated in Figure 8 and is shown in Equation 3.

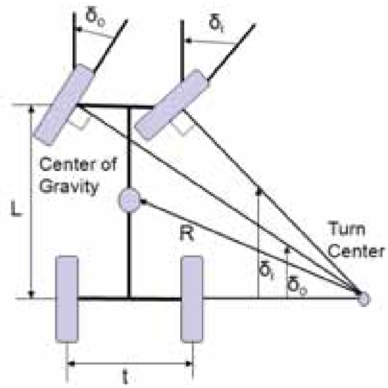


Figure 8. Illustration of Ackerman Steering Geometry

$$\delta = \arctan\left(\frac{L}{R}\right) \tag{3}$$

## 3. Control Parameters Tuning

In order to perform a fair comparison between the two algorithms, the control parameters of each algorithm were tuned to obtain optimum performance, which produces minimum overshoot, oscillation and corner cut. Tuning was carried out in simulation using Matlab as well as test run on the AGV.

Follow-the-Carrot

Follow-the-carrot algorithm performance is bounded by two control parameters, turning gain (K) and look ahead distance (LAD). Design of experiment (DOE) technique was used to prove that there is no interaction between the two parameters. Hence, they can be tuned separately.

LAD was tuned first because it was observed from DOE that it has greater effect on the overall path tracking performance. The simulation and test run results (Figure 9 and Figure 10) show similar trend where increasing LAD increases corner cut and the time taken for the AGV to return to path. When LAD is smaller than the optimum value, decreasing LAD increases overshoot at corner as well as oscillation when returning to path. Although there is resemblance between the two plots, optimum performance is obtained at different LAD value. Hence, the optimum LAD was chosen at 1.0m for simulation and 2.0 for testing on the AGV.

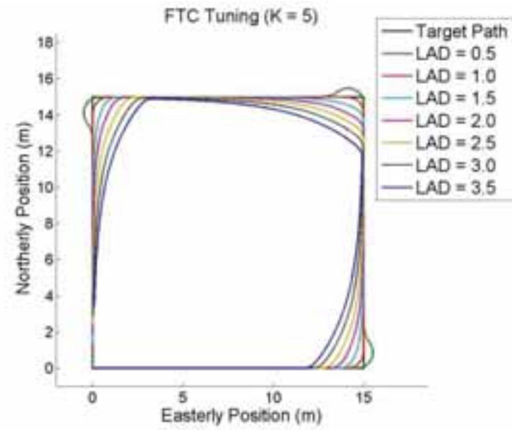


Figure 9. Simulation results of LAD tuning.

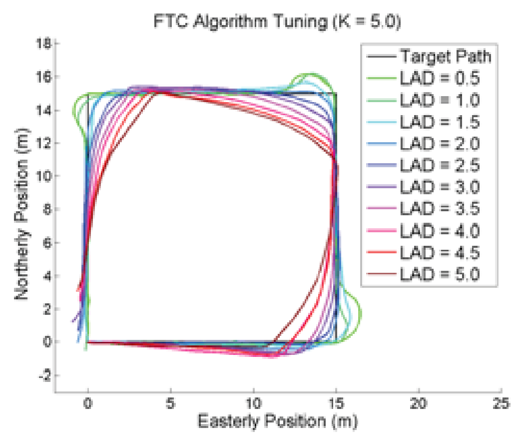


Figure 10. AGV results of LAD tuning.

Then, $K$ was tuned and results are plotted in Figure 11 and Figure 12. The results show that K has little effect on the performance. Simulation results show that when K is small, overshoot and oscillation is observed at corner, however when $K$ is greater than 5, it has no effect on the path performed. In fact, most of the path produced by the AGV while varying $K$ overlap on each other. This is limited by the minimum turning radius of the vehicle. Hence, optimum $K$ was chosen at 5 for both cases.

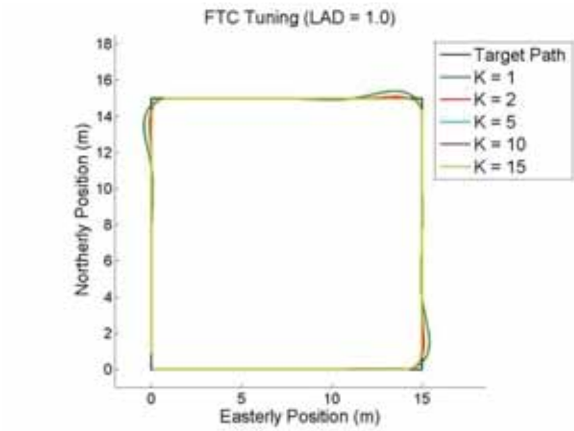


Figure 11. Simulation results of K tuning.

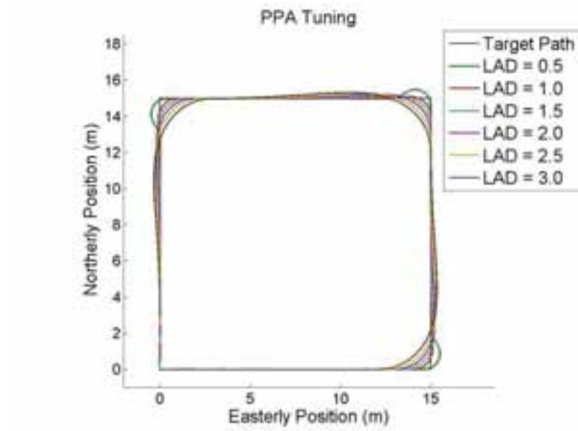


Figure 13. Simulation results of PP tuning

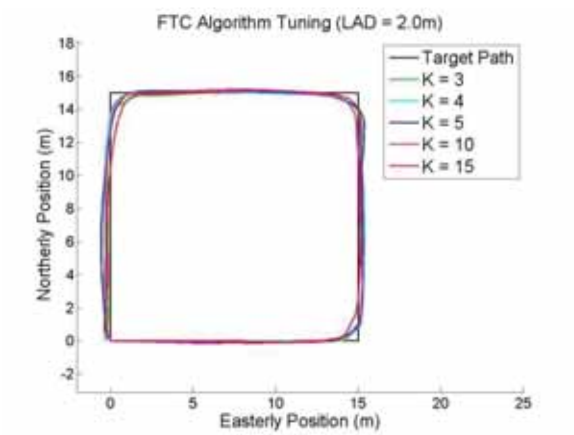


Figure 12. AGV results of K tuning.

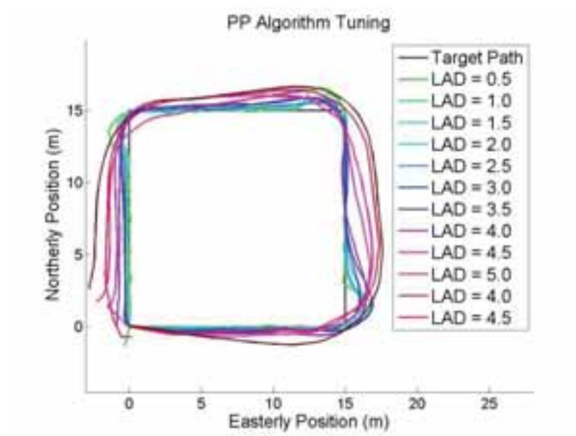


Figure 14. AGV results of PP tuning

Pure Pursuit

LAD value of pure pursuit was also tuned to achieve optimum performance. Both simulation and experimental have produced similar results (Figure 13. Simulation results of PP tuningFigure 13 and Figure 14). When LAD is small, overshoot and oscillation are observed at corner. However, when LAD is greater than a certain value, overshoot occurs and increases as LAD value increases. In fact, in AGV testing, when LAD is greater than 4.0m, the AGV struggles to return to the path. This is caused by the huge turning radius computed when the algorithm tries to connect LAP that is far away from the vehicle with a circular arc. This indicates that the algorithm is unstable when LAD is too big. Optimum LAD was chosen at 1.0m for simulation and 2.0m for AGV.

## 4. Path Tracking

Results

With the control parameters optimally tuned, both algorithms were simulated and tested on the AGV. A total of three paths were used in both simulation and AGV tests, a rectangular path, a triangular path and a semi-circular path.

For linear paths, both rectangular and triangular paths, the simulation results are shown in Figure 15 and Figure 16 where the AGV tests results are shown in Figure 17 and

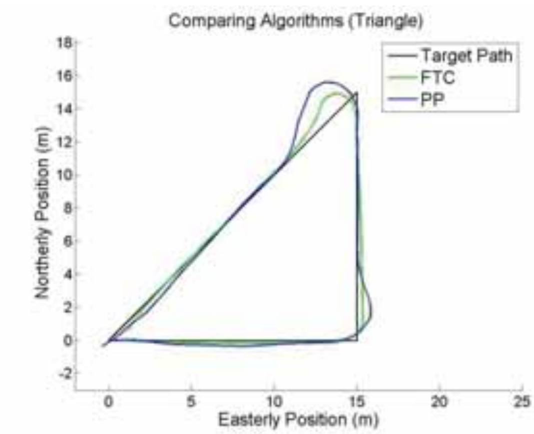


Figure 18. From the results, PP had displayed more overshoot around the corners compared to FTC in both simulation and AGV tests.

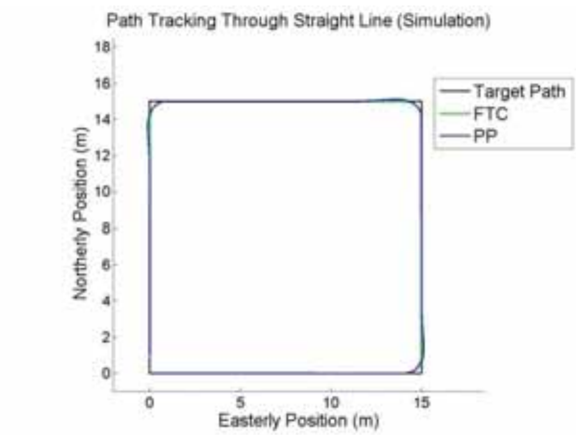


Figure 15. Simulation results of rectangular path

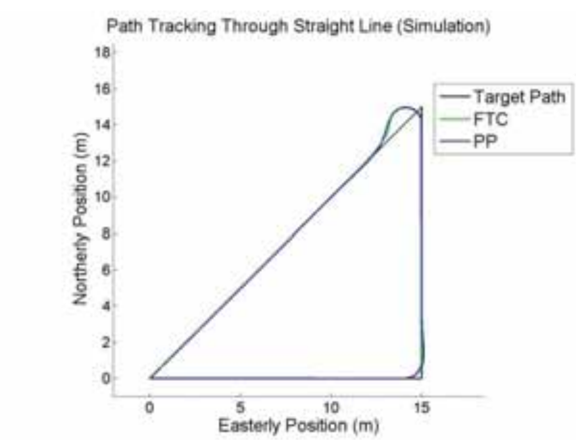


Figure 16. Simulation results of triangular path

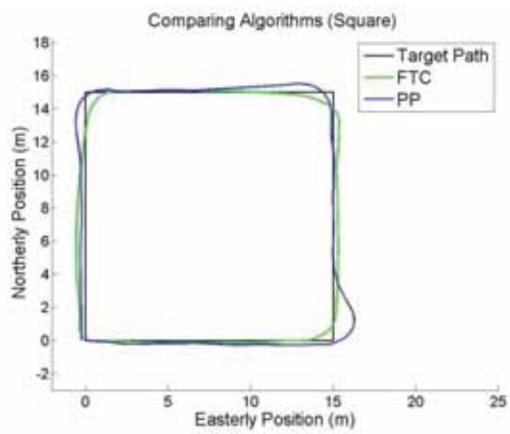


Figure 17. AGV results of rectangular path

As for semi-circular paths, the simulation result is shown in Figure 19 where the AGV test result is shown in Figure 20.

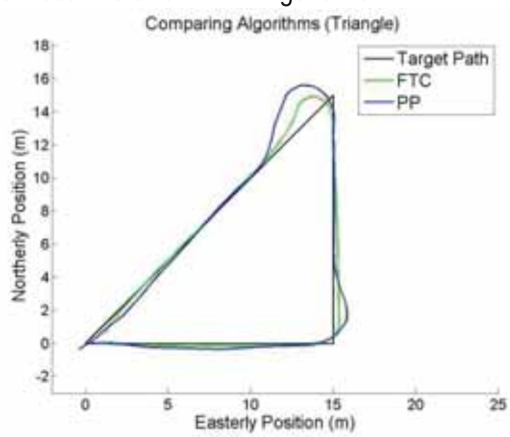


Figure 18. AGV results of triangular path

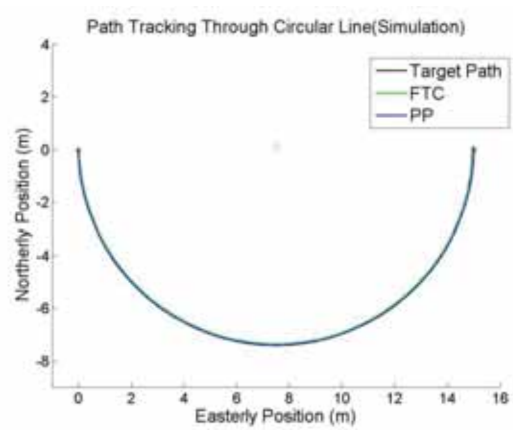


Figure 19. Simulation results of semi-circular path

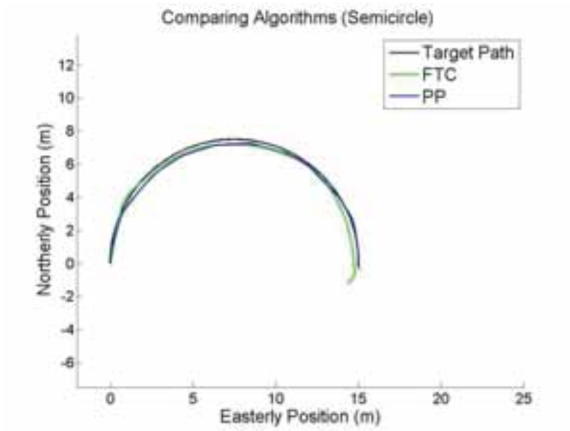

Figure 20. AGV results of semi-circular path

From the results, PP was observed to be able to track the target path more accurately with fewer paths tracking error. As for FTC, it has a higher tendency to travel on the inner side of the circular paths hence producing more error compared to PP. Path tracking error for each algorithm in different paths are summarised in Table 1.

Table 1. Average path tracking errors of both algorithms on different paths during AGV tests

| | FTC (m) | PP (m) |
|---|---|---|
| Rectangular Path | 0.2099 | 0.2794 |
| Triangular Path | 0.2304 | 0.3456 |
| Semi Circular Path | 0.3359 | 0.1406 |

Characteristics of algorithms

Both FTC and PP use different approaches to track the predetermined path given to the AGV. Due to the different concepts behind the algorithms, they displayed several unique characteristics.

FTC operates in a similar fashion as to holding a carrot in front of an animal. This algorithm uses simple calculations to determine required turning radius using the orientation error. Due to that, it is robust to external environmental disturbances as it is able to conduct path correction directly and quickly. It is also able to perform generally sharper turns, which allows the vehicle to track linear paths with less error. However, when tracking circular paths, FTC has a high tendency to travel on the inner side of circular arcs producing higher path tracking error compared to PP. FTC also requires two control parameters during operation. As a result, it is more difficult to be tuned to obtain optimum performance. On the other hand, this indicates that FTC offers better controllability to the user.

PP operates by constructing a circular arc connecting the vehicle's position and the LAP. Through this method, PP mainly produces path with turns with larger turning radius. This indicates that PP has a high tendency to produce overshoot while tracking linear paths even at optimum tuning. However, when tracking circular paths, PP is able to track the target path more accurately with less error due to its arc-based operation. In addition, PP is considerably sensitive to external disturbance as it will not directly correct its path by orientating the vehicle to its target point but to construct an arc and follow it towards the destination point. With only one control parameter, PP is easier to be tuned for optimum results. However, this also implies less controllability to the user.

## 5. Discussion

Both path tracking algorithms tested are dependent on geometry theories and the dynamic model of the AGV is not taken into consideration here. However, in this project, the AGV was driven at a slow forward velocity roughly between 0.4m/s to 1.2m/s. Hence, the effect of dynamic model can be neglected. It is also worth noting that the AGV testing data presented are obtained from the EKF which is the localised data. They do not represent the physical position of the AGV in space. Localisation error can be caused by limitation of sensor accuracy, especially the GPS receiver. Note that the accuracy of GPS receiver is sensitive to external factors such as weather, tall buildings in the surrounding as well as test location. To minimise the effect of external factor, all tests were carried out in the same location with similar weather condition. For each set of testing condition, a few test runs were performed to obtain the best performance so that random error is eliminated. With the mentioned precautions, it was sensible to assume perfect localisation is achieved when analysing path tracking performance. It should also be noted that the results discussed are particularly limited to the AGV model used in this paper. The value of optimum control parameters might vary according to vehicle specification but the general trend of performance should be similar.

## 6. Conclusions

- Pure pursuit algorithm was successfully implemented in both simulation and on the AGV.
- Both follow-the-carrot and pure pursuit algorithms were successfully simulated and tested on the AGV.
- Both algorithms were able to achieve similar path tracking performance when tuned correctly to obtain optimum control parameters.
- Path tracking performances of both algorithms depicts different characteristics and thus the choice of algorithm depends on application.

## Acknowledgements

The authors would like to thank Dr Kean Aw for the opportunity to work on this project as well as his support and guidance throughout the year. Thanks also go to Mr Logan Stuart, the Mechatronics lab technician, for his help in acquiring technical parts for the project.

## References

[1]. A. Krishnan, Upgrading of a GPS Guided Autonomous Ground Vehicle, University of Auckland, Part IV Project Report, 2012-MT25, 2012.

[2]. J.P. Jackson, Localisation and Path Tracking in a Steered-Wheel Autonomous Ground Vehicle,University of Auckland, Part IV project report, 2010-MT20, 2010.

[3]. M.L. Cheuk, Improved Path Tracking with Sensor Fusion and GPS for an Autonomous Ground Vehicle, University of Auckland, Part IV project report, 2011-MT27, 2011.

[4]. M.Lundgren, Path Tracking and Obstacle Avoidance for a Miniature Robot, Department of Computer Science, Umea University, Master's Thesis, 2003.

[5]. R. C. Coulter, Implementation of the Pure Pursuit Path Tracking Algorithm, The Robotics Institute of Camegie Mellon University, 1992.

# Object Detection and Handling for a Small Autonomous Robot

Chou Koon Goh, Carl O'Grady
The University of Auckland,
Department of Mechanical Engineering,
Mechatronics Engineering,
New Zealand

**Abstract:**
The aim of this project is to design an object handling system for a small autonomous robot that is able to handle firm foam cubes and store them on the robot. This project is part of the National Instrument Autonomous Robot Competition (NIARC) held at Swinburne University, Melbourne, Australia, on September 2013, and reached the semi-final. Research has been done to determine the best gripper mechanism to be implemented on to the mobile robot. The two main features are the camera mounted at the front for vision based object handling and the simple but robust arm and claw design. The sense approach grab software algorithm was implemented and was experimented in a controlled 2m × 2m enclosed arena with several cubes placed in random locations as required by the NIARC. The experiment showed that the algorithm was successfully implemented with a picking rate of 87.5% rate.

**Keywords:** Object Detection, Object Handling, Autonomous Robot**,** Computer Vision

## 1. Introduction

Object handling systems and autonomous robotics have been widely studied and much of this research has been about interaction in a human environment. The autonomous robot must first understand how to perceive objects and the main perception in this case is to detect certain colours and determine their distance. After achieving perception, the robot must then learn how to react in certain situations. One of the obstacles to overcome with the object handling system is that the robot should be able to autonomously move itself to the targeted object and pick it up.

This project uses the National Instruments sbRIO-9636 and LabView, which were provided by National Instruments for this design project. Vision based object handling systems are mostly used with stationary arms. For this project, a mobile object detection and handling system has been developed.

## 2. Project Objectives

The objective is broken into two parts:

### 2.1 Hardware

To design an object handling system capable of working with a mobile camera:

- The arm has to be able to move in a wide range of motion to enable it to dispose of unwanted cubes.
- The end effector has to be able to pick gold cubes and be robust to different cube orientations

### 2.2 Software

To implement a software algorithm utilising LabView and implement it onto the sbRIO-9636 that enables the robot to:

- Detect gold cubes
- Approach the gold cube through autonomous mobility
- Pick up gold cubes
- Differentiate gold cubes from other coloured cubes
- Know what to do with either gold or other coloured cubes

## 3. Hardware Design

### 3.1 Mechanical

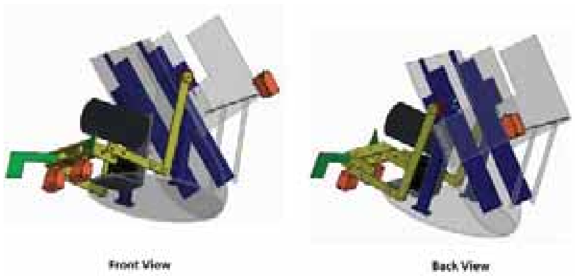


**Figure 1.** Final developed design

Figure 1 shows the side view of the overall object handling system and is colour coded for labelling purposes:

- Red - The Phototransistor sensor. (Beneath the gripper)
- Black - The laser range finder sensor. Used for navigation into the mining zone
- Grey cylinder region above laser range finder – Where the axis IP camera is mounted. This is the main sensor for detecting gold cubes.
- Blue - The loading system. The loading system is mostly mechanical and it relies on gravity to slide the stored cube to the bottom.
- Orange - Motors attached.

### 3.2 Sensors

- **Axis IP Camera**
  Axis 207W IP Camera Used for detecting gold cubes or other desired colours. The camera will be mounted as shown in the grey region shown in Figure 1.
  Factors to be considered are:
  Viewing Range: The camera has a viewing range of 55 degrees horizontal and 41.25 degrees vertical. This limitation however is overcome and will be explained in the software design section. By mounting the camera at a downward angle trigonometry can be used to overcome the lack of depth information.
- **Infra-Red Distance Sensor**
  An IR distance sensor was used to confirm cube acquisition and provide a less computational way to determine unwanted cubes

## 4 Software Design

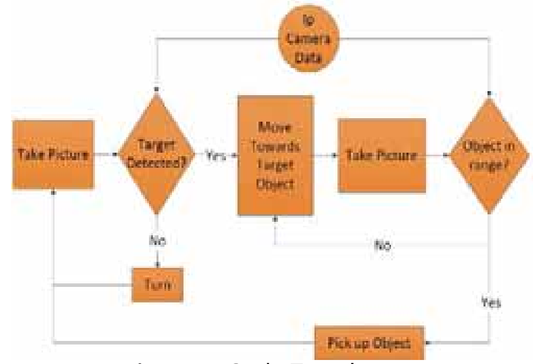


**Figure 2.** Code Function

The code uses the detect-approach-grab algorithm was based on Kragic et al. [1]. However, modifications of the algorithm will be made to suit the application. As shown in Figure 2 the robot starts by taking a picture and detects if the robot is facing towards the targeted object, if it is not, the robot will turn and take another picture until it detects the targeted object. When the target object is detected the robot will move towards the object until it gets close, when it will pick up the object and store it in the storage area shown in Figure 1 and start looking for another target object.

The target objects in this case are gold cubes. If there are multiple gold cubes detected, the robot will prioritise the closest cube. With the robot able to determine the closest cubes location, a simple PID controller is implemented to drive the robot towards the gold cube and correct its orientation error. The robot knows when to pick cubes up due to a threshold implemented in the detection code. The robot counted the number of cubes it had picked up and how many were left. This enabled it to stop when it had acquired all the cubes. The distance of the cube from the robot was first determined by Equation (2).

The vertical angle of the cube is:
$\theta_{vertical} = 0.34375 \times (60 - Top\ Y + Height)$ (1)

Distance of the cube from the Robot is:
$D = H \times \tan(\theta_{vertical} + \theta_{camera})$ (2)

The angle of the Cube from the robot is:
$\theta_{horozontal} = 0.3475 \times (X_{cube\ center\ of\ mass} - 80)$ (3)

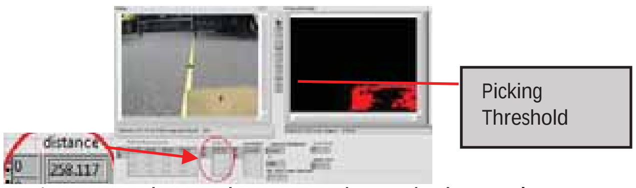


**Figure 3.** Distance incorrect when cube is too close

As the robot approaches the gold cubes, the lower part of the cube will not be seen by the camera and this means that the calculated distance will not decrease as the cube gets closer than a certain value. It can be fixed by changing the tilt of the camera but the range of the camera would then be reduced, to solve this, when the cube is too close the distance from the top of the image will be measured and when the top of the cube is below a certain point it will be determined to be close enough to pick. There has not been anything implemeanted yet to give the distance of the cube using this method.

## 5 Experiment

The testing of the object handling was based on the number of successful runs when trying to pick 4 gold cubes and how many attempts it made per run. This was tested in an enclosed area of 2m square and the 4 cubes were randomly placed around this area.
A successful pick is when the robot picked the cube and successfully stored it in the loading ramp. The number of attempts indicates the number of times when the robot closed the claw and raised the arm but did not successfully store the cube. This was tested 8 times. In this experiment, there was no human intervention as the robot autonomously moved towards the gold cubes unless there was any possible damage being done to the cubes, the environment or to the robot.
After picking up all the gold cubes the robot stopped.

## 6 Results

The object handling system has a high success rate of 87.5%. However, the robot made more attempts than needed. Ideally the number of attempts the robot made should be the same as the number of cubes in the zone for each trial.

## 7 Discussion

In different trials, the cubes were randomly placed in the enclosed area mainly for testing the picking and placing of the object in different situations. The results show that the object handling system has a high success rate. The number of attempts to pick the cube was to check the robots detection and efficiency of the object handling system.
In the experiments, some notable observations were made. The results that we have obtained from the experiment have shown that the algorithm was successfully implemented and the robot can work very well in different picking situations. One of the reasons was due to using the camera and HSV colour threshold for this method has gave very robust and accurate reading of the cube distance and angle relative to the robot.
The claw design was also robust as it was able to pick up cubes regardless of the orientation of the cube to the robots claw. The disadvantage is that it relies heavily on the robot mobility to get to the cube. The arm design used also had to be a certain distance away from the walls for it to be capable of picking successfully.

## 8 Future Work

Further development of the arm and looking at developing the second method of cube distance detection are areas for more work in this project.

## 9 Conclusion

The desired algorithm was successfully implemented on a mobile autonomous robot.

The object handling system implemented on the autonomous robot has a picking success rate of 87.5%.

The distance calculations implemented were effective providing the entire cube was visible in the image.

## Acknowledgements

I would like to express my gratitude to our supervisors, Bernard Guillermin for giving good technical advice on building a robust robot and also helping us to keep on track with the task on designing the object handling system for the autonomous robot. Kean Aw for providing technical advice on designing the robot and also for providing certain electronics components in designing the circuit for the robot.

Also our appreciation to National Instruments for providing the sbRIO-9636 and the LabView software material needed to carry on testing and developing our design. Not forgetting Ken Snow for providing the materials to construct the robot and also good advice on how the part should be manufactured. Finally, our greatest thanks to Auckland University Robotics Association (AURA) for providing materials to construct the autonomous robot

## References

[1]. Kragic, D., Björkman, M., Christensen, H. I., and Eklundh, J.-O. (2005). Vision for robotic object manipulation in domestic settings. Robotics and autonomous Systems, 52(1), pp. 85–100.

# The Autonomous Terrain Profiling Vehicle

N. Homer, F. Tinwala
The University of Auckland,
Department of Mechanical Engineering,
Mechatronics Engineering,
New Zealand

**Abstract:**
Theodolite surveying is a common practice for both land and mine surveying; however this method can be both time consuming and tedious. This technique incorporates inherent errors that can be hard to eliminate and the accuracy is largely dependent on the skills of the surveyor. With the use of Microelectromechanical Systems (MEMS) technology such as, a gyroscope, accelerometer and a magnetometer, an efficient and easier method of surveying can be developed that minimises the requirement for human operation. This paper details the development of a profiling vehicle that uses this technology to develop a 2-Dimensional cross-section of a ground profile and a bearing plot for surveying applications. By using sensor fusion algorithms such as, complimentary filter, the data from the accelerometer and gyroscope can be used to determine the inclination of the terrain. Using this with encoder data, a terrain profile is created. This project also won third prize in the International Competition of Application in Nano-Microtechnology (iCAN) held from 16th – 18th June , 2013 at Barcelona, Spain.

**Keywords:** Surveying, sensor fusion, complimentary filter, Autonomous Ground Vehicle (AGV), Microelectromechanical Systems (MEMS)

## 1. Introduction

Surveying is an important application for infrastructural development and mining. Currently within the industry, surveyors utilize theodolite surveying technology, a manually operated surveying tool that measures inclinations between two relative points [1]. Theodolite surveying therefore provides coarse discrete measurements and additionally can take a long time to set up [2, 3]. Though the theodolite is the most commonly used surveying tool and is fairly accurate, the emergence of MEMS (micro-electro-mechanical systems) sensor technology provides a gap in the market for the development of new tools for this field.

An Inertial Measurement Unit (IMU) comprising of a gyroscope, an accelerometer and a magnetometer is required to provide a profiling technique purely based on independently gathered sensory information. These sensors provide the relevant information to determine continuous inclination data over a section of land. This data can then be used to compute a graphical representation of terrain.

This project therefore explores the potential for the development of a new surveying system that utilises IMU technology on a mobile ground vehicle to achieve an independent and autonomous surveying system. The aim is to prove the concept of an alternative method of land surveying through an autonomous vehicle. To do this, focus has been given to software development, hardware development and sensor fusion computation; a method of using the data from multiple sensors and fusing them to obtain relevant data sets.

The system will be tested to determine whether this technology can provide a very high level of measurement accuracy for surveying sites and can be made a potential competitor to existing theodolite technology.

## 2. Objectives

The aims of this project are:

- To develop a system that successfully proves the concept of profiling terrain using an autonomous vehicle.
- To develop a vehicle that is interfaced wirelessly with a computer to enable the user to control the surveying vehicle from a distance.
- To display a 2D cross-section using a line graph and the bearing map using a polar plot to the user.
- To create an entire system that runs in real time to provide real time continuous measurements.
- To perform the needed hardware modifications and software developments to create the final autonomous terrain profiling vehicle.

## 3. Hardware Development

### System Hardware Architecture

**Figure 1.** The Autonomous Ground Vehicle (AGV)

The total system comprises of the following hardware components:

### Inertial Measurement Unit

A 9DOF IMU sensor stick was purchased from SparkFun Electronics to perform the tilt sensing operations. It includes the ADXL345 accelerometer, the HMC5883L compass, and the ITG-3200 gyro. The board is interfaced using the I2C protocol.

### Arduino Mega 2560 Micro Controller

The micro controller on the vehicle was replaced with the Arduino Mega 2560. This is because the board can be programmed with the Arduino programming environment. The Arduino programming environment is a simple, easy-to-use tool. This environment includes the libraries for the 9DOF IMU, making it much easier to interface all the sensors.

### Optical Quadrature Encoders

There are two custom made quadrature encoders on the two front wheels of the vehicle. A quadrature encoder works by reflecting infrared light on a series of black and white segments. The number of changes between black and white are counted and this is used to determine the distance travelled by the vehicle.

### Bluetooth Module

The vehicle and the computer communicate using Bluetooth. The Bluetooth module is the BlueSMiRF Gold. The module acts as a virtual serial interface between the two devices.

### DC Motors and Motor Drivers

There are 2 DC Motors attached to the two rear wheels of the vehicle driven by two H-Bridge L298N Motor Driver circuits. The DC Motors are geared and operate at 12V.

### Battery and Power Distribution Board

The vehicle is powered by a 16.8V battery and a power distribution board was designed to drop supply the correct voltages to the components. The voltage was dropped to 12V and 5V. In order to drop the voltage to 12V, an off the shelf linear adjustable voltage regulator was used. To drop the voltage to 5V a DC-DC converter was used. A Mean Well 5W DC-DC Regulated Single Output Converter SCW05A-05 was purchased.

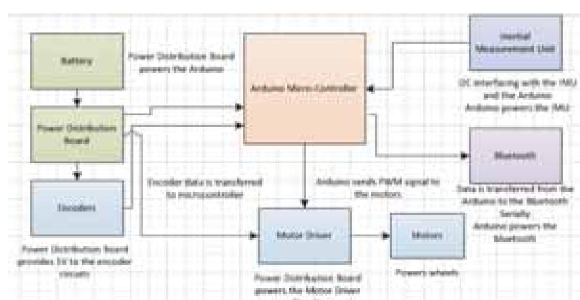


**Figure 2.** System Hardware Interaction

## 4. Software Development

### Overall Software Architecture

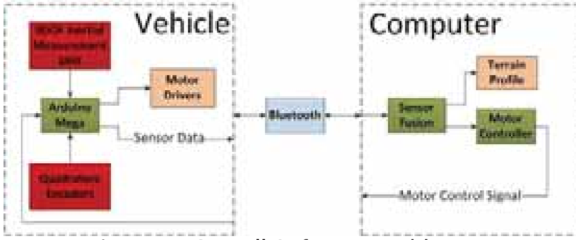


**Figure 3.** Overall Software Architecture

It was proposed that vehicle would simply send the measured data to the computer and the computer would do the processing to create the profile. This is because the computer has more processing power than the vehicle and the ability to program in higher programming languages. The computer is the master controller of the system. It sends commands to control the vehicle.

### Vehicle Software Architecture

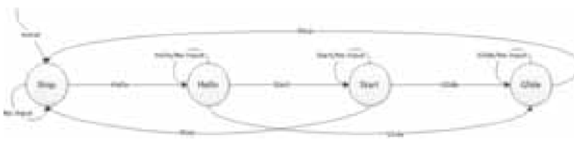

**Figure 4.** Vehicle Finite State Machine

The architecture of the vehicle is set up as a Moore finite state machine (FSM), where the computer sends the input signals to trigger the state transitions. The outputs of the states are dependent on the states only. There are four states and they are the described below:

*1. Stop/Initial* – This state is the initial state where the vehicle first starts in. In this state the motors are stopped and no data is sent to the computer.

*2. Hello* – The computer sends a 'Hello' signal to establish connection. In return the vehicle sends an acknowledgement message. This acknowledgment is proof of a connection and hence, the handshake protocol for RS-232 serial communications is satisfied [4].

*3. Start* – This is when the vehicle reads the raw data from the sensors and sends it to the computer. Then the computer sends the value of the PWM which controls the speed of the motors.

*4. Glide* – In this state, the vehicle still sends the data over but stops the motors and allows the vehicle to glide. (Used when the vehicle is travelling downhill)

### Computer Software Architecture

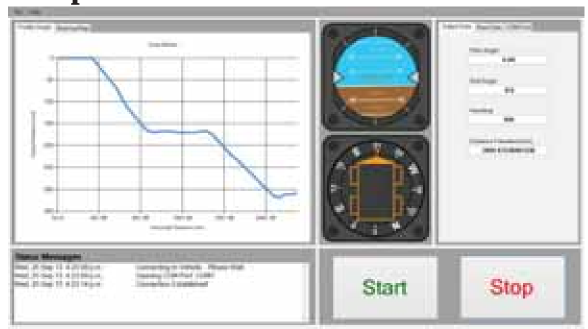


**Figure 5.** Graphical User Interface (GUI)

The following are the features and functionalities of the GUI:

- The terrain profile is shown as a line graph. This is the 2D cross section of the terrain the vehicle travelled over.
- The bearing map is within another tab. This is displayed using a polar plot. The calculated heading is plotted against the distance travelled.
- The calculated data such as, the pitch angle, roll angle, heading and distance travelled are shown in text boxes. This shows the user the calculated numbers stored in each variable.
- Attitude and Heading indicators were used to aid the user. These aircraft avionics are good visual instruments to show the how the vehicle is behaving whilst travelling over terrain.
- The 'Raw Data' tab allows the user to see the raw data sent by the vehicle. This can be used as a troubleshooting tool when issues arise.

### Sensor Fusion Algorithm

*ITG-3200 Gyro -* In order to determine the angle of tilt or inclination experienced by the sensor, the gyroscope angular velocity output signal must be integrated. The integration of the sensor data contributes to an increase in the errors produced by the sensor therefore the use of a gyro sensor for inclination readings increases the amount of gyroscopic drift [5]. In this case the effect of gyroscopic drift is more significant than the output error produced by the accelerometer drift. In order to gather information about the pitch angle changes experienced by the ground vehicle, the x-axis angular velocity has been taken for the computation of pitch. In the case of the roll angle, the y-axis gyro reading was utilised. The trapezium rule for integrating has been used to compute the angle of inclination using the MEMs Gyroscope. The data is integrated through the time interval of 38.5ms to match the time it takes to receive a new piece of data from the sensor stick.

$$\theta_{gyro} = \int_0^t \omega_z \, dt = \frac{\omega_z(t) + \omega_z(t-1)}{2} \times T$$

$where\ \omega_z(t)\ is\ the\ current\ z_{axis}\ output\ in\ rads^{-1},$
$\omega_z(t-1)\ is\ the\ previous\ output,$
$T\ is\ the\ time\ period\ between\ each\ calculation$

***ADXL345 Accelerometer -*** The ADXL345 3DOF accelerometer has been used to independently gather information about the inclinations of the terrain experienced by the ground vehicle. The accelerometer readings can be used to determine the angle of inclination by using the z and y axis components of gravity. Simple trigonometry has been used to get the final angle output from the accelerometer reading:

$$\theta_{accel} = tan^{-1}\left(\frac{g_x}{g_y}\right)$$

$where\ g_x\ is\ the\ x_{axis}\ output,$
$and\ g_y\ is\ the\ y\_axis\ output$

The computation of the sensor fusion technique was implemented on C#. The sensor data transferred over from the ground vehicle in real-time is continuously processed using the complimentary filter before outputting the data to the user through the GUI.

## Complimentary Filter

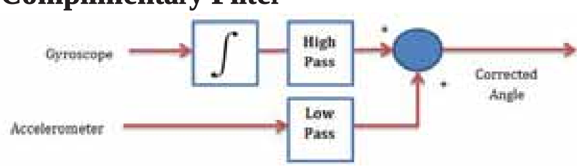


**Figure 6.** Complimentary Filter Block Diagram

The sensor fusion technique was implemented to attain an accurate output angle from the data gathered by both the gyroscope and the accelerometer. The filter of choice was the complimentary filter as it is simple and has low computation requirements compared to other sensor fusion techniques and is therefore quite fast when implemented.

This sensor fusion technique implements a high pass filter to reduce the low frequency gyroscopic drift error and a low pass filter to reduce the high frequency noise signal that distorts the accelerometer sensor readings. In this way the different spectral noises that affect each sensor is addressed. The filter then uses the summated data to determine an accurate inclination output angle from the sensors.

Both the high pass and the low pass filters are affected by the cut-off frequency. This frequency is dependent on the parameter 'a' shown below:

$$a = \frac{\tau}{\tau + \Delta t}$$

$$where\ \Delta t = sampling\ time$$
$$\tau = time\ constant$$

The time constant determines whether the accelerometer readings or the gyroscope readings are weighted more when determining the final inclination readings of the ground vehicle [6]. A larger time constant ensures that the accelerometer data is weighted more while a lower time constant places larger weighting on the gyroscope readings [6].

The parameter 'a' of the complimentary filter was determined through testing to find the most appropriate value that would give the best results for inclination data computation. The surveying program was run, while the ground vehicle was stationary. It was positioned at an angle of approximately 0.8 degrees to determine whether it effectively determined the correct output angle. The complimentary filter was found to be the most effective at 'a'=0.9.

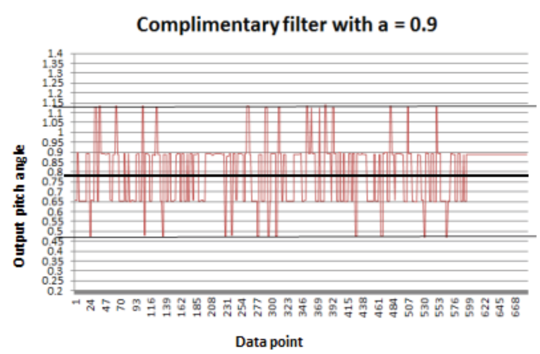


**Figure 7:** Complimentary Filter with a=0.9

The noise fluctuations in the data readings taken from the surveying system were significantly reduced to only fluctuate about ± 0.3 degrees of its true value. There was also no significant apparent drift in the sensor readings.

## Weighted Average Filter

Though the complimentary filter proved quite effective when determining the inclination readings on a static vehicle, the vehicle needed to be tested in a dynamic environment. This is when the vehicle was mobile and the motors were turned on. Through various tests that were conducted, it was found that the sensor readings were distorted due to mechanical vibration sourced from the DC motors. The vibrations significantly increased the noise in the inclination data. In order to reduce the effects of mechanical vibration on the sensor readings, a weighted average filter shown in Figure 8 was incorporated at the output of the complimentary filter.

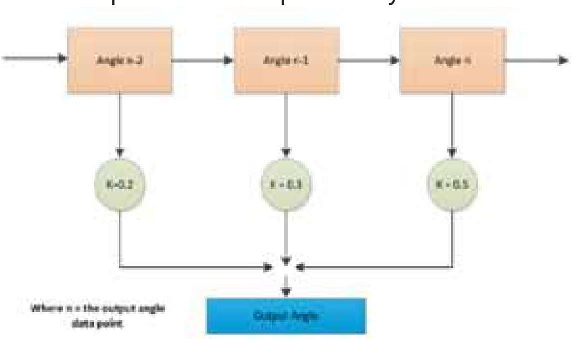


**Figure 8.** Weighted Average Filter

This significantly improved the output of the surveying system.

## 5. Testing and Results

The Autonomous Terrain Profiling vehicle was tested using the test rig shown in Figure 9. The following characteristics were tested for:

- Profile representation achieved by the system
- Accuracy of the measurements
- Repeatability of the measurements

**Figure 9.** Test platform

Figure 10 shows one result from the numerous tests that were conducted on the Autonomous Terrain Profiling vehicle compared to that of the dimensions of the test rig. The numbers on the test rig model signify the four measurement points that were considered to determine the accuracy of the terrain profile.

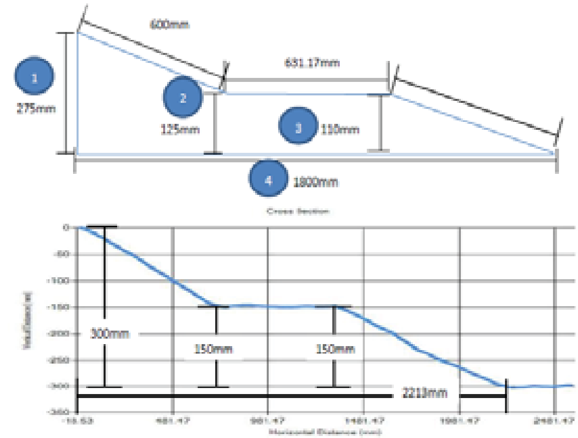


**Figure 10.** Resulting Terrain Profile

### Profile representation

As it can be seen the Autonomous Surveying System performed well at graphically presenting the three different sections of the profile. The system was very good at tracking the variations in the different sections and as it can be seen there was no evident drift in the profile.

### Accuracy

From Figure 10, it can be seen that the resulting profile shows an overall vertical decline of 300mm. However, the actual measurement determined by the surveying vehicle was 275mm. This is an error of 9.09%. The horizontal distance at the end of the third section is approximately read as 2200mm. The actual measurement was 1800mm. This is an error of 22.22%. Overall it can be seen that there is a significant amount of error attributed to the profile determined by the system.

### Repeatability

The following figures show two more tests conducted on the test rig to determine the repeatability of the initial results gathered.


**Figure 11.** Repeatability Test Results

It can be seen that all 3 profiles show 3 distinct sections representing the 3 three different sections of the test rig. From measurement 1 to measurement 2 all three profiles are approximately 150mm from the start position. This is an accurate representation. However, at the end of the third section all three profiles show different horizontal and vertical distances showing that the inaccuracy builds as the surveying system runs for long periods of time. There is not a large amount of repeatability in the tests.

## 6. Discussion

From the results shown in the section above it can be seen that the system becomes less accurate over longer distances. This is a result of the accuracy of the encoders. Since, the accuracy of the encoders is very low the accuracy of the entire system is affected. It was also noticed that the number of ticks recorded over similar distances varied contributing to lack of repeatability for the tests. This could be because the encoder is failing to detect segments. The 22.5° resolution results in a ratio of 19.2mm per tick. The resolution and accuracy of the encoders are also the reason why the repeatability is an issue. Over longer distances, the error adds up and causes greater inaccuracies. New DC motors can be purchased that have in-built encoders. These encoders have a resolution of 4331 ticks per revolution [7]. A higher resolution will allow the system to be more accurate and repeatable over longer distances.

It was also noticed that the vehicle did not move at a constant velocity over the surface. The motor control algorithm allows the vehicle to climb steep terrain and glide downhill, but it fails to keep the vehicle at constant speed. This causes the vehicle to experience accelerations other than gravity. These accelerations cause the accelerometer readings to spike due to external accelerations from the vehicle. This inaccuracy then introduces errors in the sensor fusion calculations and hence outputs inaccurate information. Further research and development is required to keep the vehicle at a constant velocity.

Overall, the system meets the objectives set out at the beginning of this project. The system has proved the plausibility of autonomously profiling terrain. Using the concepts of sensor fusion, a 2D cross-section and bearing map are created. The results show that the system can detect features in the terrain. In the experiments above, the system output distinct sections that represented distinct features in the test platform.

## 7. Recommendations for Future Work

- Upgrade the chassis to a bigger aluminium chassis. All terrain wheels with a suspension system would be ideal. This would create larger friction on the wheels and larger torque. The suspension will eliminate external noise experienced by the sensors. Furthermore, increase the damping around the IMU to remove vibrational noise from the motors.
- Purchase new DC Motors with in-built encoders and remove the old encoders [21]. This will significantly increase the accuracy of the system.
- Using the new encoders, develop a PID controller to control the velocity of the vehicle. This will also increase the accuracy and the repeatability of the system.
- Add proximity sensors around the vehicle to add obstacle avoidance.

• Integrate with GPS to log the absolute position of the vehicle.
• Add a barometer to determine the height of the vehicle above sea level.
• Research the field of smartphone sensing. The increase in smartphone technology has created more efficient ways of sensor fusion using accelerometers, gyros and compasses.
• Research the current market of surveying technologies. Contact companies that conduct surveying and gain valuable feedback to improve the project.

## Acknowledgements

We would like to thank Dr. KC. Aw for all of his support, guidance and help throughout the duration of this project.

We would also like to acknowledge the contribution and help of Bryn Edwards and Mengyie Xie throughout this year.

## References

[1]. Venkatramaiah, C. (1996) *Textbook of Surveying.* Universities Press (India), New Delhi. Pages 248-249.

[2]. Kavanagh, B. F. (2010). Introduction to Total Stations and Theodolites. In *Surveying with Construction Applications* (7th ed., pp. 99-111). New Jersey, USA: Pearson.

[3]. Cooper, M. A. (1982). *Modern theodolites and levels* (2nd ed.). London, UK: Granada.

[4]. *Interface between data terminal equipment and data communication equipment employing serial binary data interchange.* (1969). Washington, USA: Electronic Industries Association, Engineering Dept. OCLC 38637094.

[5]. *Interface between data terminal equipment and data communication equipment employing serial binary data interchange.* (1969). Washington, USA: Electronic Industries Association, Engineering Dept. OCLC 38637094.

[6]. *Stack Overflow*. [Online]. Available: http://stackoverflow.com/questions/18095785/how-to-determine-the-parameter-alpha-of-a-complementary-filter [2013, October 27]

[7]. Pololu - 67:1 Metal Gearmotor 37Dx54L mm with 64 CPR Encoder. (n.d.). Retrieved October 2, 2013, from http://www.pololu.com/catalog/product/1445

# Mechatronics Design and Heavy-Duty Omni-Directional Mecanum Mobile Robot for Research Purposes

Li Xie, Chaojie Hu
The University of Auckland,
Department of Mechanical Engineering,
Mechatronics Engineering,
New Zealand

**Abstract:**
The Mecanum wheel has been used in automated guided vehicle systems (AGVS) for many decades because of its omni-directional motion ability without wheel steering, which is particularly used in transportation in confined spaces. However its disadvantages such as slipping, skidding and poor dead-reckoning hinder its further applications in autonomous scenarios. Aiming at building a robot for research purposes, this mechatronics project was proposed to design and manufacture a heavy-duty, omni-directional and four-Mecanum-wheel mobile robot. Five design tasks - control system hardware design, electric power supply circuit design, structural mechanical design, servo motor velocity control design and software design - have been finished to successfully accomplish this robot design project. At the end of the project, all five design tasks cooperated seamlessly and the robot has been successfully constructed. The robot is able to perform smooth simple motions with loading in the tests.

**Keywords:** Mecanum wheel; Omni-directional; Heavy-duty; Mobile robot; Mechatronics design

## 1. Introduction

The Ilon Mecanum wheel was invented by Ilon in 1973 and the patent for it was then bought by the US Navy [1]. The Mecanum wheel, shown in Figure 1, is described as a conventional wheel with a designed number of rollers placed at a 45° angle around its circumference. The angled rollers provide a force towards normal to the roller rotation direction.

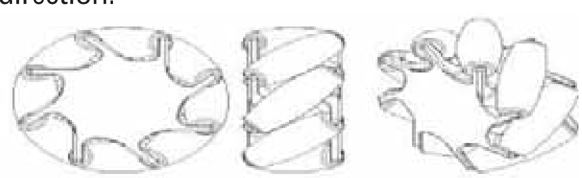

**Figure 1.** Mecanum wheel. Sourced from [2]

The combination of the different speeds and directions of each independent wheel therefore results in an omni-directional motion without wheel steering in Figure 2.

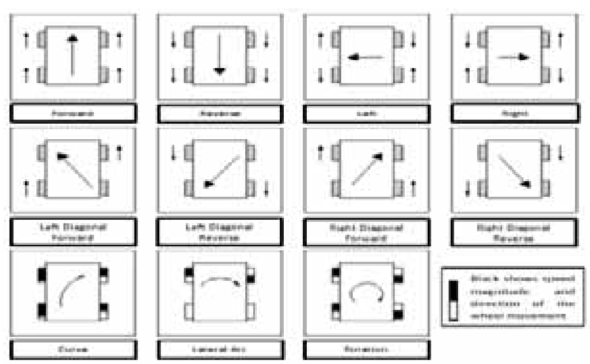

**Figure 2.** Combinational wheel actuations for general motion. Source from [3]

The Mecanum wheel's ability to provide omni-directional motion without wheel steering has advantages for the transportation of heavy objects especially in confined spaces (e.g. warehouse forklift [4]). However problems relating to Mecanum wheels such as slipping, skidding and poor dead-reckoning[5] must be solved for its further application in automated guided vehicle (AGV). These problems become even more intractable to handle when the Mecanum-wheeled vehicle is dealing with heavy-duty issues. Instead of researching using small models, a large-scale Mecanum-wheel robot with heavy-duty capability must therefore be designed and manufactured for future research, which will aim at localization sensing, autonomous navigation and optimal energy consumption.

## 2. Aim and objectives

The main aim of the project is to design and assemble a heavy-duty, omni-directional and four-Mecanum-wheel mobile robot for research purposes. The robot was specified by regarding it as a warehouse forklift and the design assumptions were made around this application. The mobile robot is able to carry a maximum weight 300 kg and has enough space for both a person to sit and a carried load to place. In addition, the robot is able to achieve simple motion in open-loop control without sensors. There are five design tasks to be done as objectives in the project:

- Control System Hardware Design
- Electric Power Supply Circuit Design
- Structural Mechanical Design
- Servo Motor Velocity Control Design
- Software Design

## 3. Control system hardware design

The control system hardware design includes the selections of controller, motor, motor drive and control panel. The final solutions were all purchased as a complete set from Beckhoff Automation, which provides compact technology for an integrated control system. A complete set of products from one company avoids incompatibility issues and a complex tuning process.

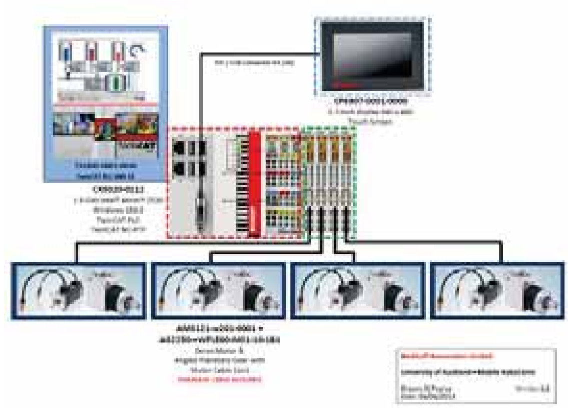

**Figure 3.** Schematic diagram of the robotic control system. Sourced from [6]

A diagram of the robotic control system hardware design is given in Figure 3. At the centre of the diagram there is an embedded PC (circled in red dot lines) with four motor drive terminals (circled in green dot lines). The embedded PC as the controller is programmed through Beckhoff software (TwinCAT) for PLC programming. Four servomotors with gear units are directly connected to the motor drive terminals. The terminals are constantly monitoring and controlling the motors. All the monitoring parameters and controlling status are displayed in the touch screen control panel (circled in blue dot lines) at the top of the schematic diagram. In addition, motor control commands are also inputted through the touch screen.

## 4. Electric power supply circuit design

All the control system hardware devices require power supply. The main purpose of the electric power supply circuit is to provide and maintain different supply voltages for each device in a safe manner. Sufficient protection must be provided to the hardware devices such embedded PC, control panel and servo motors. A complete electric power supply circuit consists of batteries, circuit breakers, voltage stabilizer and control system hardware devices.

All electric power supply circuit components are designed to be placed in the appropriate locations, as shown in Figure 4.

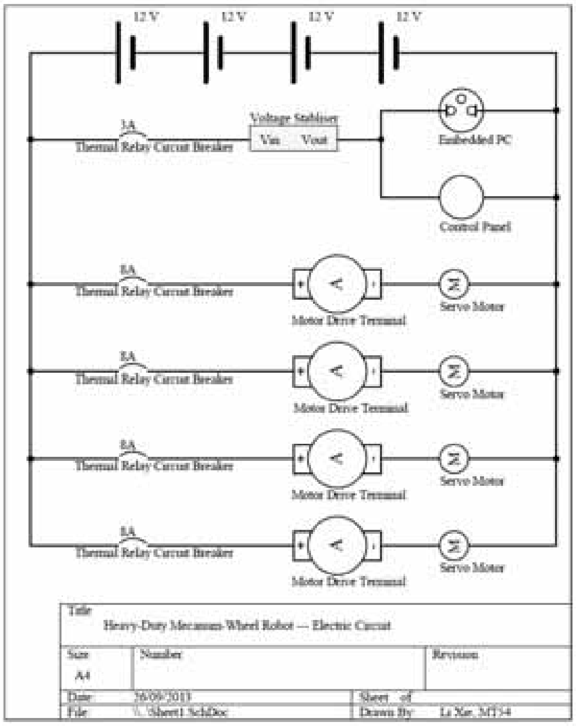


**Figure 4**. Electric power supply circuit schematic diagram

Four 12 V batteries are in series to generate 48 V voltages for servo motors. A voltage stabilizer transfers 48 V to a stable 24 V for both the embedded PC and control panel. Five thermal relays are used for overload current protection and as switches.

## 5. Structural mechanical design

The wheels, chassis, motor shaft, bearing, bearing housing and wheel hub are the important mechanical components of the structural mechanism in the robot. A complete structure is displayed in Figure 5. The chassis of the robot is designed to support up to 400 kg weight. The dimension of the chassis is 1.2 m x 0.8 m x 0.3 m. The robot is designed to work in plain ground due to the warehouse forklift assumption. So the suspension system is not included in the chassis design. The chassis is assembled by T-slotted aluminium extrusion solutions. Each of the Mecanum wheels is able to support 100kg load and it has a radius of 0.11 m.

**Figure 5.** Completed mechanical structure

As shown in the Figure 6, the motor shaft, bearing with housing and wheel hub constitute one important rotation component. The motor shaft transmits torque and rotation from the servo motor to the wheel hub. A ball bearing with housing fixes the shaft on the chassis and allows smooth rotation of the shaft.

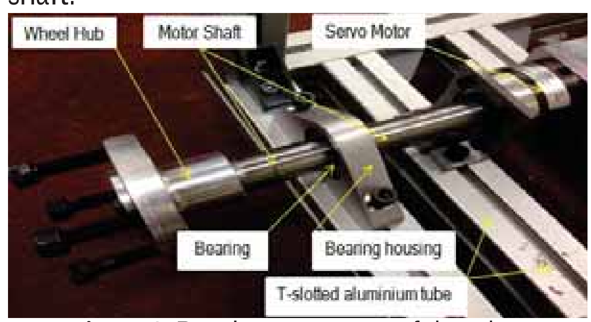


**Figure 6.** Rotation component of the robot

## 6. Servo motor velocity control design

In order to perform the optimal motor operation, a fine control system must be designed. The servo motor solution is a permanent magnet synchronous inductive motor, which is controlled in a close-loop with position, torque or velocity. Due to the nature of the Mecanum wheel, position control is useless for the motion of the robot. Velocity control is more appropriate for robot motion and is applied to the motor operation.

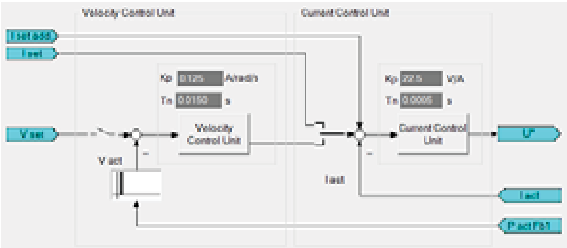


**Figure 7.** Servo motor controller block diagram overview

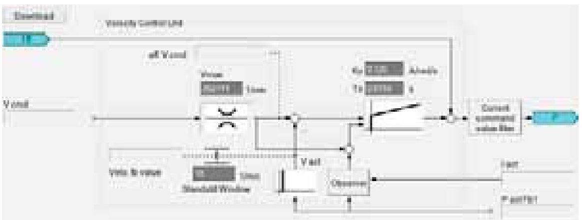

**Figure 8.** Velocity control unit block diagram

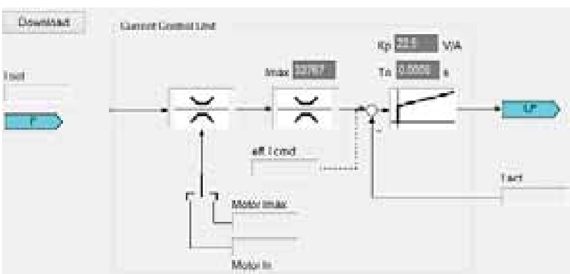


**Figure 9.** Current control unit block diagram

The servo motor velocity controller is shown in Figure 7. The controller consists of velocity control unit and the current control unit. In the block diagram, the system variables are in blue colours. Velocity error between the desired velocity and actual velocity is sent into the velocity control unit. Current error is calculated from the difference of the desired current and actual current, then regulated by the output of velocity control unit. The current control unit generates the voltage output to the servo motor. In Figure 8 and Figure 9, both input errors are eliminated in a proportional-integral (PI) controller. The controller parameters in grey are manually tuned by an 80% oscillation tuning method, which is to slowly increase one parameter until the motor begins to slightly oscillate. Then 80% of parameter at the time is the optimal value.

The motor performance is shown in Figure 10. Very little variance exists in steady state.

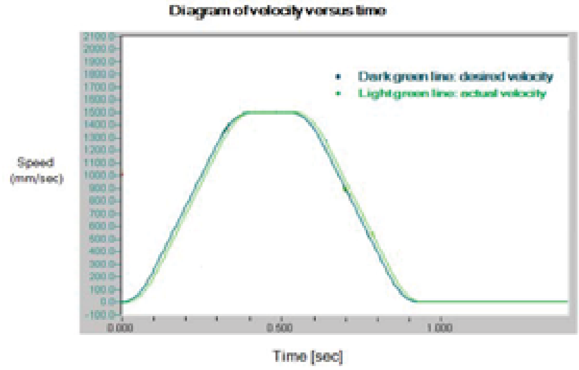


**Figure 10.** Diagram of the servo motor velocity versus time from motor tests

## 7. Software design

The Beckhoff TwinCAT software contains the programming environment TwinCAT PLC and numerical controller (NC) Axis control TwinCAT NC. The IEC61131-3 programming language is used to program PLC. A complete and sophisticated PLC programming with graphical user interface (GUI) has been finished. The system variables including the position and velocity of each wheel are dynamically displaying in the GUI, as shown in the Figure 11. All the commands are also inputted through GUI on the touch screen control panel.

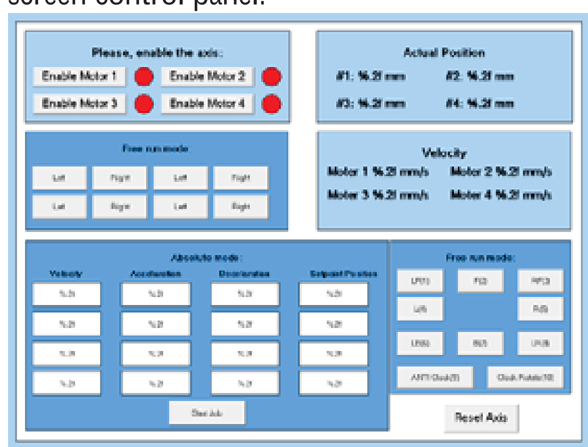


**Figure 11.** GUI of the robot control

## 8. Final design model and simple test

The robot has been successfully assembled taking into consideration all the different design requirements. Due to the limited resources of the Mechatronics lab (space, loadings and weighing tool), comprehensive assessment and testing cannot be done. The total weight of the robot is approximately 80 kg. In a simple test, the robot is able to carry one adult and provide smooth and simple motions including forward and backward movements at the desired velocity and acceleration. The assembled robot is shown in Figure 12.

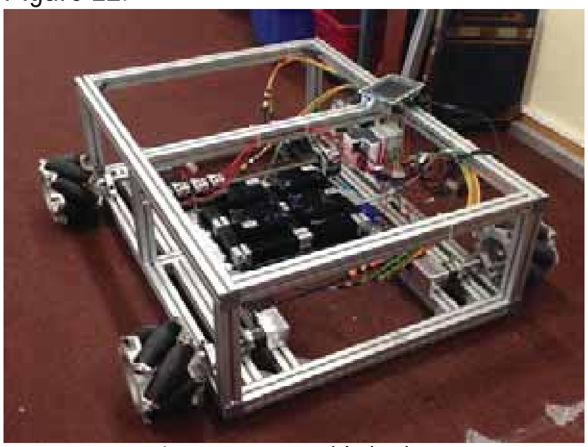

**Figure 12**. Assembled robot

## 9. Discussion

To successfully accomplish the project, five design tasks have been completed. The control system hardware design was achieved by successfully setting up a control system with products purchased from Beckhoff Automation. The electric power supply circuit design successfully provided the stable power supply to each control system hardware device with suitable protection. The structural mechanical design was well analysed and the robot mechanism met the project requirement. The servo motors operated very well with very little variance by the designed PI controller and tuning procedures. The software design was completed by a sophisticated PLC program and a GUI control panel. Robot motion can be controlled by the PLC program via the GUI. Then the robot has been successfully assembled based on these five design tasks. The robot has been tested with simple motion tests, which show enough evidence of the successful completion of the project. All five design tasks constitute a very typical and comprehensive mechatronics project. A large-scaled robot design project, which starts from the very beginning as a completely new project, is very challenging to students. However the comprehensive project did provide the students at the Department of Mechanical Engineering at the University of Auckland with much practical experience.

## 10. Conclusion

The project was successful completed and the main features are described as follows:

- A 1.2 m x 1.0 m x 0.3 m Mecanum-wheel robot with 300 kg loading capability has been designed and constructed for future research, rather than a small-scale model because slipping, skidding and low efficiency problems are more serious in the large-scale model.
- Five design tasks, including control system hardware design, electric power supply circuit design, structural mechanical design, servo motor velocity control design and software design and the robot has been successfully assembled.
- The robot is able to perform simple motions including forward and backward movements with a person sitting on top at the desired velocity and acceleration and this provides enough evidence of the successful completion of the comprehensive mechatronics project.
- The servo motor velocity control design contributes to an accurate velocity control of servo motors in a close-loop controller. A three-phase servo motor is PI-controlled in both velocity and current. An 80% oscillation tuning method is used to tune the controllers.
- The software design is based on the Beckhoff TwinCAT. The final program with PLC and NC-PTP involved, allows independent motion control of each motor with the application of GUI.

**Acknowledgements**

I would like to thank Professor Peter Xu, my project supervisor who gave peerless guidance in the project and Chaojie Hu, my best project partner and lovely friend who is hardworking and encouraging. In addition, I am very grateful for the help from Logan Stuart and Harold Tarun, the Mechatronics Lab technicians who gave lots of help in this project.

**References**

[1]. Ilon, B.E., *Wheels for a course stable selfpropelling vehicle movable in any desired direction on the ground or some other base*, 1975, US Patents number 3876255.

[2]. Diegel, O., et al. *Improved mecanum wheel design for omni-directional robots*. In *Proc. 2002 Australasian Conference on Robotics and Automation, Auckland*. 2002.

[3]. Phillips, J.G., *Mechatronic design and construction of an intelligent mobile robot for educational purposes.* Master of Technology Thesis, Massey University, Palmerston North, New Zealand, 2000. **150**.

[4]. Adăscăliţei, F. and I. Doroftei, *Practical Applications for Mobile Robots based on Mecanum Wheels-a Systematic Survey.* 2011.

[5]. Nagatani, K., et al. *Improvement of odometry for omnidirectional vehicle using optical flow information*. In *Intelligent Robots and Systems, 2000.(IROS 2000). Proceedings. 2000 IEEE/RSJ International Conference on* 2000. Takamatsu, Japan: IEEE.

[6]. *Beckhoff Information System. Beckhoff Automation*. Retrieved April 2013; Available from: http://infosys.beckhoff.com/index_en.htm.